

## Estimating the black hole spin for the X-ray binary MAXI J1820+070

Xueshan Zhao,<sup>1,2</sup> Lijun Gou,<sup>1,2</sup> Yanting Dong,<sup>1,3</sup> Youli Tuo,<sup>4</sup> Zhenxuan Liao,<sup>1,2</sup> Yufeng Li,<sup>1,2</sup> Nan Jia,<sup>1,2</sup> Ye Feng,<sup>1,2</sup> and James F. Steiner<sup>5</sup>

<sup>1</sup>Key Laboratory for Computational Astrophysics, National Astronomical Observatories, Chinese Academy of Sciences, Datun Road A20, Beijing 100012, China

<sup>2</sup>School of Astronomy and Space Sciences, University of Chinese Academy of Sciences, Datun Road A20, Beijing 100049, China

<sup>3</sup>Zhejiang Institute of Modern Physics, Department of Physics, Zhejiang University, 38 Zheda Road, Hangzhou 310027, China

<sup>4</sup>Key Laboratory of Particle Astrophysics, Institute of High Energy Physics, Chinese Academy of Sciences, 19B Yuquan Road, Beijing 100049, People's Republic of China

<sup>5</sup>Harvard-Smithsonian Center for Astrophysics, Cambridge, MA 02138, United States

### ABSTRACT

MAXI J1820+070 is a newly-discovered black hole X-ray binary, whose dynamical parameters, namely the black hole mass, the inclination angle and the source distance, have been estimated recently. *Insight*-HXMT have observed its entire outburst from March 14th, 2018. In this work, we attempted to estimate the spin parameter  $a_*$ , using the continuum-fitting method and applying a fully-relativistic thin disk model to the soft-state spectra obtained by *Insight*-HXMT. It is well known that  $a_*$  is strongly dependent on three dynamical parameters in this method, and we have examined two sets of parameters. Adopting our preferred parameters:  $M = 8.48^{+0.79}_{-0.72} M_\odot$ ,  $i = 63^\circ \pm 3^\circ$  and  $D = 2.96 \pm 0.33$  kpc, we found a slowly-spinning black hole of  $a_* = 0.14 \pm 0.09$  ( $1\sigma$ ), which give a prograde spin parameter as majority of other systems show. While it is also possible for the black hole to have a retrograde spin (less than 0) if different dynamical parameters are taken.

*Keywords:* *Insight*-HXMT, black hole physics, X-rays:binaries, X-rays: individual (MAXI J1820+070)

### INTRODUCTION

The spin is a crucial parameter of a black hole, which is helpful to understand the driving mechanism of the relativistic jets (Blandford & Znajek 1977), to explore the fundamental physics around the black hole (Wong et al. 2012), to test the predictions of general relativity (Bambi & Barausse 2011, Bambi & Modesto 2013, Tripathi et al. 2020). We usually use a dimensionless parameter  $a_*$  to represent the spin, defining  $a_* \equiv a/M = cJ/GM^2$ , where  $M$  and  $J$  represent the black hole mass and angular momentum. In the traditional electromagnetic (EM) domain, we can only estimate the spin with some indirect techniques since the spin only makes itself notable via the general relativistic (GR) effect within a small region around the event horizon<sup>1</sup>. So far, there have developed two widely-used methods to measure the spin parameter of accreting stellar-mass black holes: (1) the continuum-fitting method, which models the shape of the thermal emission from the accretion disk (Zhang et al. 1997); (2) the reflection-fitting method, which models the red wing of the relativistically-broadened and asymmetric Fe K $\alpha$  line (Fabian et al. 1989, Reynolds & Nowak 2003).

The key process of the spin measurements is to estimate the radius of the inner disk  $r_{\text{in}}$  ( $r_{\text{in}} \equiv cR_{\text{in}}/GM$ ).  $R_{\text{in}}$  is assumed to be equal to the radius of the innermost stable circular orbit  $R_{\text{ISCO}}$  (Shafee et al. 2008b, Reynolds & Fabian 2008, Penna et al. 2010, Kulkarni et al. 2011, Noble et al. 2009, Noble et al. 2010, Noble et al. 2011), which is a monotonic function of the dimensionless spin parameter  $a_*$ , decreasing from  $6R_g$  ( $R_g$  is the gravitational radius, which is defined as  $R_g = GM/c^2$ ) to  $1R_g$  as the spin increases from  $a_* = 0$  to  $a_* = 1$  (Bardeen et al. 1972).

Corresponding author: Xueshan Zhao, Lijun Gou  
xszhao@nao.cas.cn, lgou@nao.cas.cn

<sup>1</sup> It is noted that both the gravitational wave (Abbott et al. 2020) and Event Horizon Telescope (EHT) observations can directly constrain the black hole spin. The gravitational wave observations have provided spin constraints for tens of merging black hole systems. As to EHT, it can only resolve the event horizons for supermassive black holes rather than stellar mass black holes (Event Horizon Telescope Collaboration et al. 2019).

MAXI J1820+070 is a newly-discovered transient source. Its optical counterpart, ASASSN-18ey, was discovered by the All-Sky Automated Survey for SuperNovae (ASAS-SN, Shappee et al. 2014) on March 6th, 2018 at R.A. =  $18^{\text{h}}20^{\text{m}}21.^{\text{s}}9$  dec. =  $+07^{\circ}11'07.''3$  (J2000) (Tucker et al. 2018). In X-ray, it was found by the Monitor of All-sky X-ray Image (MAXI, Matsuoka et al. 2009) on March 11st, 2018 (Kawamuro et al. 2018). Since discovery, the X-ray outburst of MAXI J1820+070 displayed a fast increase, and then a slow decay (MJD 58200-MJD 58290) in flux. The source underwent its first re-brightening (MJD 58290-MJD 58305) and then dropped sharply as transiting to the soft state. The source stayed in the soft state for over 2 months (till around MJD 58380). After around MJD 58400, the source faded away into quiescence. During the entire eruption, this source showed all of the standard accretion state (Remillard & McClintock 2006): the thermal dominant state (TD), or the high/soft state (HSS); the low/hard state (LHS); the steep power law (SPL) state (the so-called intermediate state in some literature). In order to ensure the reasonable application of the continuum-fitting method, we focus on spectra dominated by thermal accretion disk component avoiding the interference introduced by the strong Comptonization component. Based on the previous works, the continuum-fitting method is only reliably applied to a thin accretion disk, i.e., the bolometric Eddington-scaled luminosity  $l = L(a_*, \dot{M})/L_{\text{Edd}} < 0.3$  (equivalent to the aspect ratio  $H/R < 0.05$ ; Shafee et al. 2008a).

In the continuum-fitting method, one determines  $r_{\text{in}}$  by fitting the X-ray thermal continuum from the accretion disk to the Novikov-Thorne thin disk model (Novikov & Thorne 1973). As a nonrelativistic approximation, given that the disk luminosity  $L \approx 2\pi D^2 F (\cos i)^{-1} \approx 4\pi R_{\text{ISCO}}^2 T_{\text{eff}}^4$  (where  $F$ ,  $T_{\text{eff}}$ ,  $D$ ,  $i$  indicate the X-ray flux, the effective temperature, the distance to the source and the inclination angle), we have  $r_{\text{ISCO}}^2 \approx F/(2 T_{\text{eff}}^4 (\cos i)^{-1} D^2 M^{-2})$ . Therefore three dynamical parameters, namely the black hole mass  $M$ , the disk inclination  $i$  and the source distance  $D$ , are crucial for estimating the spin. As we know,  $a_*$  is inversely proportional to  $R_{\text{ISCO}}/M$  (Bardeen et al. 1972), so that a higher mass will lead to a higher  $a_*$ . Besides, we can see that the higher the inclination or the distance is, the higher the  $R_{\text{ISCO}}/M$  is, hence the smaller the spin is.

There have been systematic measurements to determine these three parameters. Torres et al. (2019) reported a mass function  $f(M) \equiv (M_1 \sin i)^3 / (M_1 + M_2)^2 = 5.18 \pm 0.15 M_{\odot}$  (where  $M_1$  and  $M_2$  indicate the masses of the black hole and the donor star), dynamically confirming a black hole harboring in this binary. Assuming a provisional mass ratio  $q \equiv M_2/M_1 = 0.12$ , they constrained the binary inclination to be  $69^{\circ} \lesssim i \lesssim 77^{\circ}$  and derived a black hole mass in the range of  $7\text{-}8 M_{\odot}$ . Atri et al. (2020) calculated the distance to be  $D = 2.96 \pm 0.33$  kpc via the measurement of the radio parallax<sup>2</sup>, using the Very Long Baseline Array (VLBA) and the European Very Long Baseline Interferometry (VLBI) Network. Further they used the distance and estimated the jet inclination angle and the black hole mass to be  $63^{\circ} \pm 3^{\circ}$  and  $9.2 \pm 1.3 M_{\odot}$  (adopting  $q = 0.12$ ), respectively. A few months later, Torres et al. (2020) analyzed intermediate resolution optical spectroscopy, leading to a direct and accurate determination of  $q = 0.072 \pm 0.012$ . Their constraint to the binary inclination is  $66:2 < i < 80:8$  based on the detection of eclipse and measurements of the accretion disk radius at the time of the optical spectroscopy, ignoring the disk vertical structure. The inclination angle derived in this way should represent the orbital inclination angle, and the corresponding black hole mass is  $5.96 M_{\odot} < M < 8.06 M_{\odot}$ . Adopting  $63^{\circ} \pm 3^{\circ}$  (Atri et al. 2020), which could be consistent with the inclination angle of the inner accretion disk, the black mass would be  $M = 8.48_{-0.72}^{+0.79} M_{\odot}$ , with uncertainties quoted at  $1\sigma$ . For the continuum-fitting method, although it is typically assumed that the orbital inclination angle is aligned with the one for the inner accretion disk, it is found that there exists some misalignments in some systems (Fragos et al. 2010, Walton et al. 2016). Therefore, it is better to use the inclination angle which is more close to the one of the inner disk. In our case, we adopt  $M = 8.48_{-0.72}^{+0.79} M_{\odot}$ ,  $i = 63^{\circ} \pm 3^{\circ}$  and  $D = 2.96 \pm 0.33$  kpc as our favored and primary parameter set to constrain the spin of MAXI J1820+070 via the continuum-fitting method. As a complement, we also discussed the spin parameter for the alternative parameter set in the discussion section.

Many previous work have studied the characteristics of MAXI J1820+070, especially, the behaviour of inner disk radius (which implies the spin) of the black hole. Kara et al. (2019) performed spectra and temporal analysis on MAXI J1820+070, suggesting that as the hard state began to transit softward, the corona reduced in the spatial extent, while the inner disk radius was stable and approximately  $\sim 2 R_{\text{g}}$ . Bharali et al. (2019) fitted spectra obtained by Swift and NuSTAR in the hard state, constrained the inner disk radius and the disc inclination angle to be  $5.1_{-0.7}^{+1.0} R_{\text{g}}$  and  $29.8_{-2.7}^{+3.0} \text{ }^{\circ}$  ( $3\sigma$ ). By investigating the spectra evolution of the entire outburst using data from MAXI and Swift, Shidatsu et al. (2019) showed that the state transition occurred at its first re-brightening phase, suggesting that it is

<sup>2</sup> The radio parallax measurement of  $0.348 \pm 0.033$  mas is consistent with the value of  $0.31 \pm 0.11$  mas estimated by Gaia-DR2. The distance estimated from the Gaia parallax is  $3.46_{-1.03}^{+2.18}$  kpc based on an exponentially decreasing space density prior (Gandhi et al. 2019)

not determined by the mass accretion rate alone. They gave the constraint of the inner disk to be  $R_{\text{in}} = 77.9 \pm 1.0 (D/3 \text{ kpc})(\cos i / \cos 60^\circ)^{-1/2}$  km during the high/soft state, with applying a combined correction factor of 1.18, for both the stress-free boundary condition and the color-temperature correction (Kubota et al. 1998). Buisson et al. (2019) analyzed data obtained by NuSTAR during the hard state, reporting a small stable inner radius, which implies a low-to-moderate-spin black hole. Fabian et al. (2020) discovered an excess emission between 6-10 keV during the soft state observed by NuSTAR and NICER, which can be well-modelled by an additional blackbody component BBODY. They explained this excess to be the emission from the edge of the plunge region where matter begins to fall into the black hole. Both Fabian et al. (2020) and Buisson et al. (2019) reported that if the inner disk inclination lies between  $30^\circ$ - $40^\circ$ , then the spin lies in the range of  $\pm 0.5$ . However, there has been no specific work to measure the spin of the black hole in MAXI J1820+070. Therefore, in this paper, we attempt to estimate the spin of this source by the continuum-fitting method.

This paper is organized as follows. In Section 2, we describe our observations and data reduction. In Section 3, we report our spectral analysis and fit results. Discussion and conclusion are showed in Section 4.

## OBSERVATIONS AND DATA REDUCTION

The *Hard X-ray Modulation Telescope* (HXMT, also named *Insight*)<sup>3</sup> was successfully launched on June 15th, 2017. There are three main detectors onboard *Insight*-HXMT<sup>4</sup>: the low energy X-ray telescope (LE, 1-15 keV, SCD, 384 cm<sup>2</sup>); the medium energy X-ray telescope (ME, 5-30 keV, Si-Pin, 952 cm<sup>2</sup>); the high energy X-ray telescope (HE, 20-250 keV, NaI(Tl)/CsI(Na), 5100 cm<sup>2</sup>) (Liu et al. 2020, Zhang et al. 2020, Chen et al. 2020, Cao et al. 2020). As a collimated telescope, it has a negligible pile-up effect, which is suitable to observe bright source such as MAXI J1820+070. It began fixed-point observations for MAXI J1820+070 on March 14th, 2018 (MJD 58191), and monitored the whole outburst of this source until October 21st, 2018 (MJD 58412).

Spectra were extracted using *Insight*-HXMT Data Analysis Software (HXMTDAS) v2.02 following a standard procedure. Only spectra from events that belong to the small FoV ( $1.6^\circ \times 6^\circ$  for LE and  $1^\circ \times 4^\circ$  for ME) were extracted. The background was measured by the blind detectors. Below 7 keV, the diffuse X-ray background is dominant while the particle background dominates above 7 keV (Guo et al. 2020, Liao et al. 2020). We estimated the level of the source contamination using HXMT Bright Source Warning Tool<sup>5</sup>, finding no other interference source (with the flux ratio of the interference source to MAXI J1820+070 no more than 0.1) in the FoVs during observations. We simply used observations from LE and ME detectors, given that these instruments have already provided adequate energy coverage and that the extremely low net counts rate in HE. The spectra were rebinned using GRPPHA with at least 100 counts per new bin. We also added systematic errors due to uncertainties of the instrumental responses and background estimation: 1% for LE and 2% for ME (Chen et al. 2020, Cao et al. 2020). Spectral analysis was performed on XSPEC v12.10.1. In this work, we analyzed 2-10 keV for LE and 10-25 keV for ME.

## SPECTRAL ANALYSIS

### *Non-Relativistic Models*

Figure 1 displays HXMT observations of MAXI J1820+070 during the 2018 outburst. As an empirical choice, we ignored spectra with hardness larger than 0.5, since our targets are the spectra dominated by thermal emission.

We first applied a preliminary non-relativistic model on these spectra, which is expressed as CONSTANT\*TBABS\*SIMPL\*DISKBB (hereafter, NR). The equivalent hydrogen column density in TBABS was fixed to  $0.15 \times 10^{22} \text{ cm}^{-2}$  to account for the Galactic absorption (Uttley et al. 2018). Model CONSTANT is used for coordinating calibration differences between the two detectors. We fixed the normalization of LE to 1, and the normalization of ME to 0.95 (Details will be addressed in Section 4). In the empirical Comptonization model SIMPL, the parameter  $f_{\text{sc}}$  calculates the fraction of the thermal seed photons that are scattered into the power-law tail (Steiner et al. 2009b). Steiner et al. (2009a) suggested that the inner disk radius (i.e. the spin) remains stable to within a few percent as long as  $f_{\text{sc}} \lesssim 25\%$ . Thereafter it became a widely-utilized spectral selection criteria in the continuum-fitting measurements of the spin. Because SIMPL redistributes seed photons to both lower and higher energies where the response matrices of HXMT are limited, we extended the sampled energies to 0.1-100 keV on XSPEC (see the appendix of Steiner et al.

<sup>3</sup> <http://www.hxmt.org>

<sup>4</sup> <http://www.hxmt.org/index.php/enhome/enabouthxmt/160-hard-x-ray-modulation-telescope>

<sup>5</sup> See the proposal software page in <http://proposal.ihep.ac.cn/soft/soft2.jspx>, and see the detailed instructions in <http://proposal.ihep.ac.cn/soft/soft2help.jspx>

2009b). In the non-relativistic multicolors black body model DISKBB, two crucial parameters are estimated, namely the temperature ( $T_{\text{in}}$ ) and the radius ( $R_{\text{in}}$ ) of the inner accretion disk.

The fit results to NR model are listed in Table 2. For NR, It can be seen obviously that the  $f_{\text{sc}}$  of these spectra all satisfy  $f_{\text{sc}} \lesssim 25\%$ , with the central values ranging from 1.4% to 18.6%. The temperature at inner disk radius  $T_{\text{in}}$  shows a small decline, lying in a range of 0.758-0.478 keV with the average value of 0.681 keV. The normalization of DISKBB is defined as  $(R_{\text{app}}/D_{10})^2 \cos i$ , where  $R_{\text{app}}$  is the apparent inner disk radius in unit of km. As defined in Kubota et al. (1998), the realistic inner disk radius  $R_{\text{in}} = \xi f R_{\text{app}}$ , where  $\xi$  is a correction factor for the stress-free inner boundary condition and  $f$  is the spectral hardening factor. We assumed a combined correction factor of 1.18 (see Kubota et al. 1998 for detail) following Shidatsu et al. (2019) in order to better compare with their results. Adopting  $M = 8.48^{+0.79}_{-0.72} M_{\odot}$ ,  $i = 63^{\circ} \pm 3^{\circ}$  and  $D = 2.96 \pm 0.33$  kpc, we calculated the inner edge of the disk  $R_{\text{in}}$  in the unit of  $R_{\text{g}}$  (the gravitational radius  $R_{\text{g}} \equiv GM/c^2 = 12.55$  km for  $M = 8.48 M_{\odot}$ ). The best-fitting value of  $R_{\text{in}}$  varies slightly from  $5.16R_{\text{g}}$  to  $6.36R_{\text{g}}$ . The averaged  $R_{\text{in}}$  is  $5.58R_{\text{g}}$ . The value of  $R_{\text{in}}$  estimated from DISKBB implies a small spin parameter. However, probably owing to the weak Comptonization component and the lower counts rate in  $E > 10$  keV, we were unable to constrain the photon index  $\Gamma$  of SP25-52 (this will be addressed in later).

### Relativistic Models

Next, we substituted DISKBB (Mitsuda et al. 1984, Makishima et al. 1986) with KERRBB2 (McClintock et al. 2006). The model is expressed as CONSTANT\*TBABS\*SIMPL\*KERRBB2 (hereafter, RM). KERRBB2 is a fully-relativistic thin disk model and is the combination of BHSPEC (Davis et al. 2005) and KERRBB (Li et al. 2005). This model reads in a pair of look-up tables for the spectral hardening factor  $f$  ( $f \equiv T_{\text{col}}/T_{\text{eff}}$ ) estimated by BHSPEC corresponding to two typical values of the viscosity parameter  $\alpha$ : 0.1 and 0.01.  $a_*$  decreases slightly as  $\alpha$  increases, so that throughout this work, we adopt  $\alpha = 0.01$  in order to make a more conservative limitation. Fit results for  $\alpha = 0.1$  are listed in Table 4. A comparison of Tables 3 and 4 reveals that  $\alpha = 0.01$  gives systematically larger values of  $a_*$ , with a difference typically  $\sim 0.05$ . Specifically, referring to Shidatsu et al. (2019), the parameter  $\Gamma$  of SP25-52 is fixed to 2.5, a representative value for the soft state. For other spectra, we allowed  $\Gamma$  to vary.

The best-fit results are showed in Table 3. In RM, the values of  $f_{\text{sc}}$  in SP55-57 and SP61 ( $25.37\% \pm 0.24\%$ ,  $25.21\% \pm 0.24\%$ ,  $25.89\% \pm 0.29\%$ ,  $27.78\% \pm 0.21\%$ ) are slightly above 25%. And the value of  $f_{\text{sc}}$  in SP58-60 ( $14.79\% \pm 0.22\%$ ,  $15.73\% \pm 0.18\%$ ,  $18.75\% \pm 0.20\%$ ) are significantly larger than that of other 54 spectra. It means that the strength of the Comptonization component in SP1-54 is faint, contributing less than about 10% of the total emission. The spin measurement using the continuum-fitting method based on those 54 spectra will be more robust. In fact, in SP55-61, MAXI J1820+070 underwent the state transition. Shidatsu et al. (2019) divided these 7 spectra into the intermediate state (IM).

Therefore, we treated these spectra as our ‘‘gold’’ spectra, mainly basing our analysis and error analysis on them although almost all the spectra meet the selection criteria  $f_{\text{sc}} \lesssim 25\%$ . Meanwhile, SP55-61 (hereafter, ‘‘silver’’ spectra) were also analyzed just as reference. In Table 2 and Table 3, we used horizontal lines to distinguish the ‘‘gold’’ spectra.

For all the ‘‘gold’’ spectra, our model provides a good fit, with the reduced  $\chi^2_{\nu}$  varying between 0.88-1.35. A representative plot of the unfolded spectrum is given in Figure 2. The best-fit value of  $a_*$  lies in the range from 0.016 to 0.253, with the mean of 0.153, confirming a slowly-spin black hole in MAXI J1820+070.

As we mentioned earlier, in order to have a successful application of the continuum-fitting method, it is important to ensure a disk with the bolometric Eddington-scaled luminosity  $l < 0.3$ . For MAXI J1820+070, it is clear that our selected ‘‘gold’’ spectra satisfy this standard, with  $l$  ranging from 0.056 to 0.150.

### Error Analysis

The errors quoted in Table 2 and Table 3 are only due to the statistic uncertainties estimated via XSPEC. The confidence level is 90%. As mentioned in Section 1, the error budget of  $a_*$  is dominated by the combined observational uncertainties of  $M$ ,  $i$  and  $D$ . Herein the Monte Carlo (MC) simulation was performed for error analysis. The steps of error analysis are described as following: for each individual spectrum, (1) assuming independent and Gaussian distributed<sup>6</sup>, we generate 3000 sets of  $(M, i, D)$ . (2) we calculate look-up tables of  $f$  for these parameter sets. (3) we re-fit the spectrum 3000 times with these  $(M, i, D)$  to determine the histograms of  $a_*$ , from which we finally decide the error of  $a_*$ .

<sup>6</sup> Previous work has confirmed that if we generate parameter sets via the mass function, the results will be roughly the same and the difference between these two methods will be nearly negligible (Zhao et al. 2020).



We made MC simulations on 54 “gold” spectra. Histograms of  $a_*$  are plotted in Figure 3, and the summed histogram is showed in Figure 4. Adopting the histogram, we arrived at the final value of  $a_* = 0.14 \pm 0.09$  ( $1\sigma$ ).

## DISCUSSION

### *effect of varying $\Gamma$ and normalization*

Normally we expect that if we fix the normalization of LE to 1, and then the normalization of ME will also be 1. However, due to the effects of systematic errors, there are minor differences between the calibration of the two detectors (Li et al. 2020), and during fitting process, the relative differences may change slightly (empirically, as for *Insight*-HXMT, within the range of 0.85 to 1.15 is considered as reasonable). We have tried to let the normalization vary between 0.95 to 1.05, however it always peg at its lower limitation 0.95 probably due to the weak Comptonization component, so that we fix the normalization of ME to 0.95.

We tested the effect of different  $\Gamma$  and norm on  $a_*$ , and fit results are presented in Table 6. It is showed that  $a_*$  decreases by  $\Delta a_* = 0.053$  as  $\Gamma$  increases from 2.10 to 2.90 (with norm frozen at 0.95), and increases by  $\Delta a_* = 0.017$  as norm varies from 0.95 to 1.05 (with  $\Gamma$  fix at 2.50).

### *effect of different parameter configurations*

As we mentioned above, the inclination is a crucial input parameter and has an obvious degeneracy with the spin. In previous section, we have the estimated the spin by assuming the jet inclination angle  $i = 63^\circ \pm 3^\circ$ , and the black hole mass  $M = 8.48_{-0.72}^{+0.79} M_\odot$ . We also constrained the spin for the case that the inclination angle ranges between  $66:2 < i < 80:8$ . Referring to Figure 5, the spin parameter decreases as the mass decreases or the inclination increases (See Section 1 for qualitative analysis), therefore we used  $i = 66:2$  and  $M = 8.06 M_\odot$  to constrain the upper limit of the spin for Torres’s parameters. The fit results are shown in Table 5. The best-fit values of this set of parameters (within a range of -0.276 to 0.036 and only eleven spectra have a spin larger than zero) are lower than that of our adopted parameters, so that Torres’s parameter configuration may leads to a retrograde black hole, which needs to be checked with the precise system parameters in the future. In addition, assuming  $M = 8.06 M_\odot$ , the spin will peg to its lower limit -0.99 in KERRBB2 if the inclination is above  $76^\circ$ . The critical value of  $i$ , which will lead to a spin of -0.99, is  $67^\circ$  for  $M = 5.96 M_\odot$ .

In applying the continuum-fitting method, the inclination  $i$  is supposed to be the inclination angle of the inner disk, which, however, is hard to be estimated in practice (In the future, the X-ray polarization method may provide more accurate constraints on it). Usually the strategy is to use the orbital inclination or jet inclination as the proxy, instead. Some previous work on fitting the reflection component reported a small misalignment between the inner accretion disk and the binary orbital plane (Fragos et al. 2010, Walton et al. 2016), which can be interpreted by a warp in the disk. In this work, we preferred the spin result for adopting the jet inclination angle as the inner disk inclination, however, more consistent and accurate dynamical parameters are required for the detailed spin measurements in the future.

As a caveat, it is noted that all the spin measurements from the continuum-fitting method (Liu et al. 2008, Gou et al. 2009, Gou et al. 2010, Steiner et al. 2011, Steiner et al. 2012, Gou et al. 2014, Steiner et al. 2014, Chen et al. 2016, Steiner et al. 2016) basically suggested positive spin values, and there has been no clear observational evidence for the existence of retrograde black holes. Morningstar et al. (2014) initially reported a retrograde spin for the black hole in Nova Muscae 1991:  $a_* = -0.25_{-0.64}^{+0.05}$  (90% confidence level). However, Chen et al. (2016) found a moderately high value of spin,  $a_* = 0.63_{-0.19}^{+0.16}$  ( $1\sigma$  confidence level) after the system parameters were updated consistently, and rule strongly against a retrograde value:  $a_* > 0.17$  ( $2\sigma$  or 95.4% confidence level).

## CONCLUSION

In this work, we have presented a methodology of the spin measurements for the newly-observed black hole X-ray binary MAXI J1820+070 using *Insight*-HXMT spectra. Mainly because the spin of the black hole strongly depends on the measurement of the disk inclination, the black hole mass and the distance, the large uncertainty of the dynamical parameters makes it difficult to critically evaluate its spin. For MAXI J1820+070, we have discussed two scenarios. Preferring to consider the jet inclination as the inner accretion disk inclination angle, adopting  $M = 8.48_{-0.72}^{+0.79} M_\odot$ ,  $i = 63^\circ \pm 3^\circ$  and  $D = 2.96 \pm 0.33$  kpc, we deduce a value of  $a_* = 0.14 \pm 0.09$  ( $1\sigma$ ), showing that the black hole in this system is rotating slowly. Besides, when the parameter ranges  $5.96 M_\odot < M < 8.06 M_\odot$  and  $66:2 < i < 80:8$  are applied, the black hole are more likely to have a retrograde spin.

Shidatsu et al. (2019) estimated the inner edge of the accretion disk in the HSS to be  $R_{\text{in}} = 77.9 \pm 1.0 (D/3 \text{ kpc})(\cos i / \cos 60^\circ)^{-1/2}$  km. Using  $M = 8.48_{-0.72}^{+0.79} M_\odot$ ,  $i = 63^\circ \pm 3^\circ$  and  $D = 2.96 \pm 0.33$  kpc, the black hole in MAXI J1820+070 is near non-rotating, which is basically compatible with our constrain of  $a_* = 0.14 \pm 0.09$  ( $1\sigma$ ). In addition, it is noted that the reflection spectral fit to the NuSTAR prefers a smaller inner disk inclination between  $30^\circ$ - $40^\circ$  and the spin range between -0.5 and 0.5 (Bharali et al. 2019, Buisson et al. 2019, Fabian et al. 2020). However, if the disk inclination is set around  $70^\circ$ , the spin derived from the same soft-state NuSTAR spectra would be almost maximally retrograde ( $a_* < -0.95$ , Fabian et al. 2020). In any event, we hope future observations could help improve the dynamical parameters, hence putting a tighter constraints on the spin parameters.

#### ACKNOWLEDGMENTS

This work made use of the data from the *Insight*-HXMT mission, a project funded by China National Space Administration (CNSA) and the Chinese Academy of Sciences (CAS). The authors thank supports from the National Program on Key Research and Development Project (Grant No. 2016YFA0400800 and 2016YFA0400801) and from the NSFC (U1838201 and U1838202). L.J.G. acknowledges the support by the National Program on Key Research and Development Project (Grant No. 2016YFA0400804), and by the NSFC (U1838114), and by the Strategic Priority Research Program of the Chinese Academy of Sciences (XDB23040100).

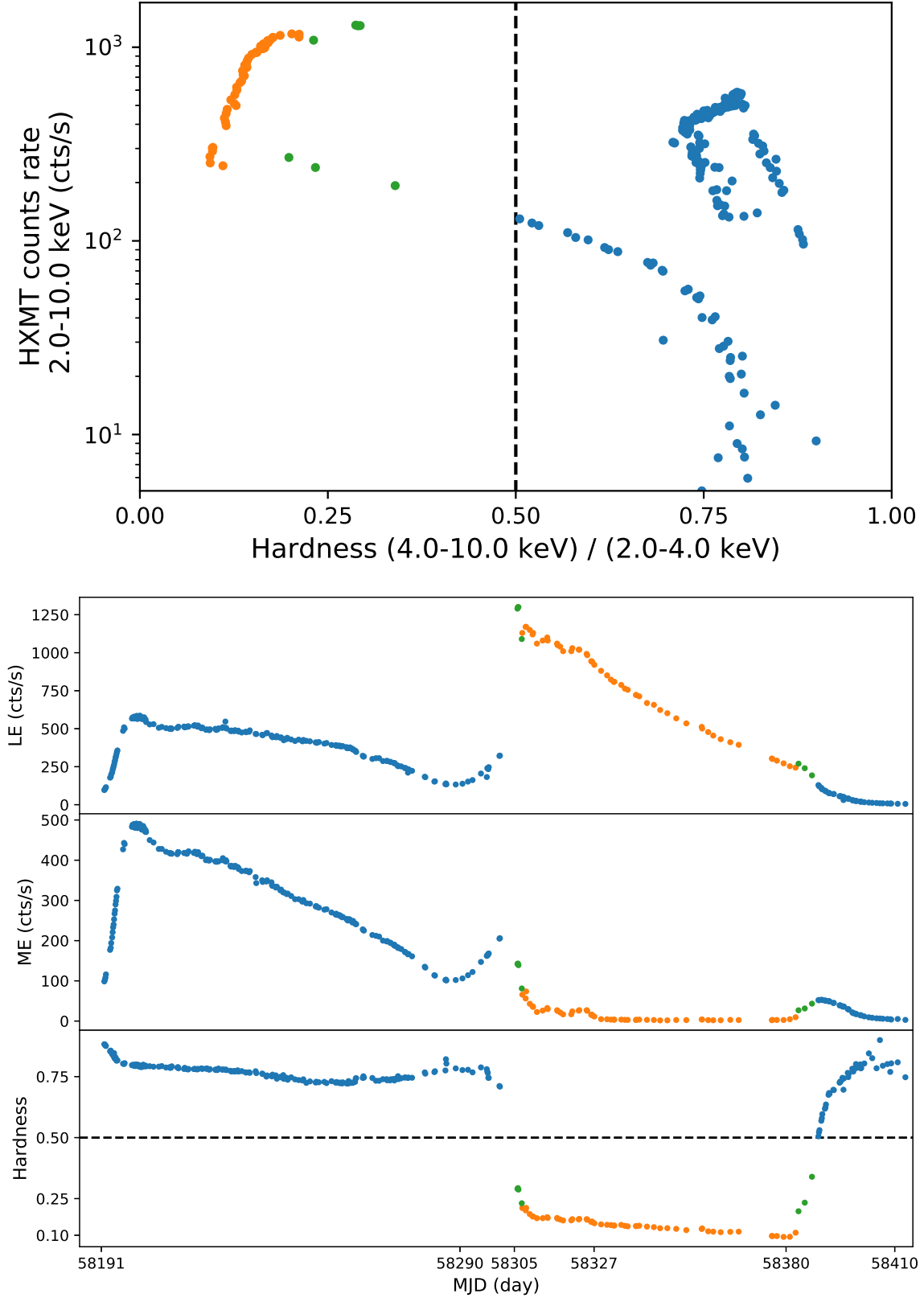


**Figure 1.** *Insight*-HXMT observations of MAXI J1820+070 covering its entire outburst. From top to bottom: the hardness-intensity diagram (HID), LE lightcurve, ME lightcurve, the evolution of the hardness ratio. The black dashed lines indicate the hardness ratio is 0.5. The blue points represent that the source is in the low/hard state, which are not analyzed in this paper. The orange and green symbols indicate observations with smaller and larger  $f_{sc}$ , respectively.

**Table 1.** *Insight*-HXMT Observational Journal of MAXI J1820+070<sup>a</sup>

Number	ObsID	MJD	Start Time	End Time	exposure(s)	State <sup>b</sup>
1	P011466108401	58305.86277	2018-07-06T20:41:17	2018-07-06T23:48:23	1674 & 2155	IM
2	P011466108402	58305.99270	2018-07-06T23:48:23	2018-07-07T03:12:37	1374 & 2556	IM
3	P011466108403	58306.13453	2018-07-07T03:12:37	2018-07-07T06:22:11	810 & 1658	IM/HSS
4	P011466108501	58307.05589	2018-07-08T01:19:23	2018-07-08T04:43:34	1211 & 2014	IM/HSS
5	P011466108502	58307.19769	2018-07-08T04:43:34	2018-07-08T09:24:42	695 & 1534	IM/HSS
6	P011466108601	58308.11641	2018-07-09T02:46:32	2018-07-09T06:14:59	747 & 1114	IM/HSS
7	P011466108602	58308.26117	2018-07-09T06:14:59	2018-07-09T10:51:44	539 & 1799	IM/HSS
8	P011466108702	58309.25513	2018-07-10T06:06:17	2018-07-10T09:07:54	479 & 1423	IM/HSS
9	P011466108801	58310.03858	2018-07-11T00:54:27	2018-07-11T04:17:01	1556 & 1343	IM/HSS
10	P011466108802	58310.17925	2018-07-11T04:17:01	2018-07-11T07:24:09	898 & 941	IM/HSS
11	P011466108901	58311.23160	2018-07-12T05:32:24	2018-07-12T10:29:02	931 & 2358	HSS
12	P011466109001	58312.82233	2018-07-13T19:43:03	2018-07-14T00:44:39	2134 & 2934	HSS
13	P011466109101	58314.08167	2018-07-15T01:56:30	2018-07-15T05:23:05	1002 & 1027	HSS
14	P011466109102	58314.22513	2018-07-15T05:23:05	2018-07-15T09:07:27	1195 & 1968	HSS
15	P011466109201	58316.79946	2018-07-17T19:10:07	2018-07-17T22:15:11	1077 & 1903	HSS
16	P011466109202	58316.92798	2018-07-17T22:15:11	2018-07-18T01:39:17	1305 & 1272	HSS
17	P011466109301	58317.66130	2018-07-18T15:51:10	2018-07-18T20:44:08	1077 & 3420	HSS
18	P011466109401	58318.45692	2018-07-19T10:56:52	2018-07-19T15:52:51	1257 & 3160	HSS
19	P011466109501	58320.71167	2018-07-21T17:03:42	2018-07-21T20:59:14	3039 & 2818	HSS
20	P011466109503	58321.00778	2018-07-22T00:10:06	2018-07-22T02:50:58	479 & 760	HSS
21	P011466109601	58322.76842	2018-07-23T18:25:25	2018-07-23T22:17:50	2298 & 2554	HSS
22	P011466109602	58322.92982	2018-07-23T22:17:50	2018-07-24T02:28:17	1270 & 1777	HSS
23	P011466109701	58324.95915	2018-07-25T23:00:04	2018-07-26T02:47:29	1564 & 2244	HSS
24	P011466109702	58325.11707	2018-07-26T02:47:29	2018-07-26T05:27:31	1583 & 1776	HSS
25	P011466109801	58326.22091	2018-07-27T05:17:00	2018-07-27T09:01:17	2454 & 2360	HSS
26	P011466109802	58326.37666	2018-07-27T09:01:17	2018-07-27T12:12:12	2453 & 2228	HSS
27	P011466109803	58326.50924	2018-07-27T12:12:12	2018-07-27T14:55:38	2213 & 1981	HSS
28	P011466109901	58327.08413	2018-07-28T02:00:03	2018-07-28T06:50:58	2544 & 3874	HSS
29	P011466110001	58328.94229	2018-07-29T22:35:48	2018-07-30T03:26:25	2523 & 4027	HSS
30	P011466110101	58330.60005	2018-07-31T14:22:58	2018-07-31T19:13:23	2261 & 4219	HSS
31	P011466110201	58331.66060	2018-08-01T15:50:10	2018-08-01T20:40:32	3700 & 3544	HSS
32	P011466110301	58332.45593	2018-08-02T10:55:26	2018-08-02T14:35:40	2101 & 4263	HSS
33	P011466110302	58332.60887	2018-08-02T14:35:40	2018-08-02T18:56:37	2573 & 3701	HSS
34	P011466110401	58334.51027	2018-08-04T12:13:41	2018-08-04T15:55:25	2829 & 4762	HSS
35	P011466110701	58335.50424	2018-08-05T12:05:00	2018-08-05T16:55:15	4219 & 5276	HSS
36	P011466110801	58336.29941	2018-08-06T07:10:03	2018-08-06T12:00:50	1841 & 3871	HSS
37	P011466110901	58338.55235	2018-08-08T13:14:17	2018-08-08T16:58:34	3286 & 4320	HSS
38	P011466110902	58338.70810	2018-08-08T16:58:34	2018-08-08T19:40:25	1137 & 1704	HSS
39	P011466111001	58339.48006	2018-08-09T11:30:11	2018-08-09T16:20:53	3044 & 4386	HSS
40	P011466111201	58341.60057	2018-08-11T14:23:43	2018-08-11T19:20:41	2514 & 3491	HSS
41	P011466111301	58343.52242	2018-08-13T12:31:11	2018-08-13T17:21:47	2155 & 3185	HSS
42	P011466111401	58345.24557	2018-08-15T05:52:31	2018-08-15T10:43:08	2692 & 3519	HSS
43	P011466111501	58347.23405	2018-08-17T05:35:56	2018-08-17T10:26:31	2514 & 3516	HSS
44	P011466111601	58349.68682	2018-08-19T16:27:55	2018-08-19T21:18:31	1735 & 2693	HSS
45	P011466111701	58352.47157	2018-08-22T11:17:57	2018-08-22T16:08:32	1648 & 2758	HSS
46	P011466111801	58356.71551	2018-08-26T17:09:14	2018-08-26T20:09:34	599 & 700	HSS
47	P011466111802	58356.84074	2018-08-26T20:09:34	2018-08-27T01:15:46	180 & 658	HSS
48	P011466111901	58358.50582	2018-08-28T12:07:17	2018-08-28T16:57:46	1542 & 3007	HSS
49	P011466112001	58359.89813	2018-08-29T21:32:12	2018-08-30T02:23:11	1317 & 1938	HSS
50	P011466112101	58361.95323	2018-08-31T22:51:33	2018-09-01T03:42:27	1594 & 3417	HSS
51	P011466112201	58364.60463	2018-09-03T14:29:34	2018-09-03T19:20:11	958 & 1976	HSS
52	P011466112301	58366.92445	2018-09-05T22:10:06	2018-09-06T01:27:46	406 & 2095	HSS
53	P011466112401	58376.07197	2018-09-15T01:42:32	2018-09-15T05:26:46	1834 & 2182	HSS
54	P011466112402	58376.22769	2018-09-15T05:26:46	2018-09-15T08:08:25	539 & 941	HSS
55	P011466112501	58377.46444	2018-09-16T11:07:41	2018-09-16T15:58:08	3111 & 2702	HSS
56	P011466112601	58379.32135	2018-09-18T07:41:38	2018-09-18T12:35:16	2655 & 2825	HSS
57	P011466112701	58381.04584	2018-09-20T01:04:54	2018-09-20T05:55:25	2076 & 2251	IM
58	P011466112801	58382.63775	2018-09-21T15:17:15	2018-09-21T20:10:31	1900 & 1990	IM
59	P011466112901	58383.43367	2018-09-22T10:23:23	2018-09-22T15:16:09	3638 & 3029	IM
60	P011466113001	58385.15798	2018-09-24T03:46:23	2018-09-24T08:36:49	2910 & 2894	IM
61	P011466113101	58387.14719	2018-09-26T03:30:51	2018-09-26T08:21:12	3694 & 3042	IM

NOTE—<sup>a</sup>The log of *Insight*-HXMT observations analyzed in this work. In columns 2–7, we show the following information, respectively: observation ID; MJD; the start time of the observations; the end time of the observations; the effective exposure times in units of second for LE and ME; accretion states.

<sup>b</sup>We adopted the states defined in [Shidatsu et al. \(2019\)](#). "IM" and "HSS" represent the intermediate and high/soft state, respectively. It is noted that [Buisson et al. \(2019\)](#) classified spectra 3-10 as HSS.



**Table 2.** Best-fit parameters for spectra with the model CONSTANT\*TBABS\*SIMPL\*DISKBB ( $M = 8.48 M_{\odot}$ ,  $i = 63^{\circ}$  and  $D = 2.96$  kpc)

Number	ObsID	SIMPL		DISKBB		Reduced $\chi^2_{\nu}$	$\chi^2$ /d.o.f.
		$\Gamma$	$f_{\text{sc}}$	$T_{\text{in}}$	$R_{\text{in}}$		
1	P011466108502	2.36 ± 0.02	0.067 ± 0.001	0.748 ± 0.002	5.28 ± 0.58	1.64	1460.3 / 893
2	P011466108601	2.48 ± 0.02	0.064 ± 0.002	0.743 ± 0.002	5.49 ± 0.60	1.47	1313.5 / 893
3	P011466108602	2.23 ± 0.01	0.059 ± 0.001	0.752 ± 0.002	5.29 ± 0.58	1.26	1085.9 / 862
4	P011466108702	2.27 ± 0.02	0.036 ± 0.001	0.753 ± 0.002	5.36 ± 0.58	1.35	1098.7 / 816
5	P011466108801	2.41 ± 0.02	0.037 ± 0.001	0.743 ± 0.001	5.53 ± 0.51	1.43	1340.6 / 940
6	P011466108802	2.35 ± 0.03	0.033 ± 0.001	0.745 ± 0.002	5.48 ± 0.55	1.33	1157.1 / 872
7	P011466108901	2.18 ± 0.03	0.017 ± 0.001	0.758 ± 0.001	5.16 ± 0.47	1.29	1103.0 / 855
8	P011466109001	2.31 ± 0.02	0.024 ± 0.001	0.751 ± 0.001	5.33 ± 0.44	1.69	1611.1 / 952
9	P011466109101	2.45 ± 0.03	0.035 ± 0.001	0.738 ± 0.002	5.55 ± 0.55	1.24	1086.2 / 876
10	P011466109102	2.24 ± 0.02	0.025 ± 0.001	0.748 ± 0.001	5.37 ± 0.48	1.40	1247.7 / 893
11	P011466109201	2.26 ± 0.02	0.023 ± 0.001	0.748 ± 0.001	5.31 ± 0.49	1.42	1243.1 / 875
12	P011466109202	2.43 ± 0.03	0.028 ± 0.001	0.743 ± 0.001	5.39 ± 0.51	1.28	1137.8 / 891
13	P011466109301	2.16 ± 0.03	0.016 ± 0.001	0.751 ± 0.001	5.25 ± 0.46	1.44	1244.8 / 863
14	P011466109401	2.20 ± 0.03	0.014 ± 0.001	0.750 ± 0.001	5.21 ± 0.45	1.46	1274.5 / 870
15	P011466109501	2.56 ± 0.03	0.023 ± 0.001	0.741 ± 0.001	5.35 ± 0.43	1.56	1498.3 / 963
16	P011466109503	2.42 ± 0.04	0.026 ± 0.002	0.736 ± 0.002	5.46 ± 0.62	1.09	791.6 / 724
17	P011466109601	2.38 ± 0.02	0.027 ± 0.001	0.735 ± 0.001	5.44 ± 0.46	1.49	1420.8 / 952
18	P011466109602	2.34 ± 0.02	0.027 ± 0.001	0.734 ± 0.001	5.44 ± 0.51	1.43	1272.2 / 889
19	P011466109701	2.40 ± 0.02	0.030 ± 0.001	0.728 ± 0.001	5.51 ± 0.50	1.50	1375.2 / 918
20	P011466109702	2.41 ± 0.02	0.029 ± 0.001	0.727 ± 0.001	5.50 ± 0.50	1.53	1391.2 / 912
21	P011466109801	2.57 ± 0.03	0.023 ± 0.001	0.727 ± 0.001	5.43 ± 0.46	1.42	1322.1 / 932
22	P011466109802	2.63 ± 0.03	0.026 ± 0.001	0.724 ± 0.001	5.47 ± 0.47	1.51	1410.5 / 932
23	P011466109803	2.77 ± 0.03	0.028 ± 0.001	0.724 ± 0.001	5.47 ± 0.49	1.40	1283.1 / 919
24	P011466109901	2.66 ± 0.03	0.019 ± 0.001	0.726 ± 0.001	5.42 ± 0.45	1.40	1289.8 / 924
25	P011466110001	4.05 ± 0.07	0.047 ± 0.003	0.713 ± 0.002	5.52 ± 0.55	1.19	1077.8 / 902
26	P011466110101	3.78 ± 0.08	0.032 ± 0.003	0.718 ± 0.001	5.37 ± 0.52	1.22	1076.5 / 885
27	P011466110201	4.50 ± 0.07	0.075 ± 0.005	0.699 ± 0.002	5.60 ± 0.57	1.19	1110.8 / 932
28	P011466110301	4.50 ± 0.09	0.066 ± 0.005	0.700 ± 0.002	5.55 ± 0.61	1.14	997.6 / 875
29	P011466110302	4.50 ± 0.09	0.066 ± 0.005	0.698 ± 0.002	5.59 ± 0.60	1.12	1000.0 / 893
30	P011466110401	4.50 ± 0.07	0.078 ± 0.005	0.697 ± 0.002	5.52 ± 0.59	1.15	1042.1 / 903
31	P011466110701	4.50 ± 0.07	0.071 ± 0.004	0.694 ± 0.002	5.52 ± 0.55	1.25	1175.5 / 941
32	P011466110801	4.50 ± 0.09	0.068 ± 0.006	0.691 ± 0.002	5.55 ± 0.64	1.19	1017.9 / 854
33	P011466110901	5.00 ± 0.17	0.105 ± 0.008	0.680 ± 0.002	5.60 ± 0.64	1.03	915.7 / 891
34	P011466110902	4.50 ± 0.11	0.077 ± 0.008	0.687 ± 0.003	5.47 ± 0.71	0.91	707.6 / 780
35	P011466111001	4.50 ± 0.05	0.109 ± 0.006	0.675 ± 0.002	5.65 ± 0.63	1.61	1454.8 / 902
36	P011466111201	4.50 ± 0.07	0.098 ± 0.006	0.675 ± 0.002	5.50 ± 0.63	1.46	1274.3 / 871
37	P011466111301	5.00 ± 0.21	0.104 ± 0.009	0.672 ± 0.003	5.53 ± 0.70	0.91	798.0 / 875
38	P011466111401	4.50 ± 0.10	0.065 ± 0.006	0.672 ± 0.002	5.44 ± 0.61	1.07	921.6 / 865
39	P011466111501	4.50 ± 0.07	0.090 ± 0.006	0.662 ± 0.002	5.52 ± 0.65	1.36	1176.2 / 862
40	P011466111601	4.50 ± 0.07	0.104 ± 0.007	0.648 ± 0.002	5.66 ± 0.73	1.33	1078.6 / 813
41	P011466111701	4.50 ± 0.10	0.080 ± 0.007	0.647 ± 0.002	5.58 ± 0.73	0.98	781.9 / 798
42	P011466111801	4.15 ± 0.12	0.084 ± 0.010	0.637 ± 0.004	5.65 ± 0.92	1.02	547.1 / 537
43	P011466111802	4.50 ± 0.14	0.147 ± 0.023	0.614 ± 0.008	6.04 ± 1.43	1.05	446.7 / 424
44	P011466111901	4.50 ± 0.09	0.095 ± 0.008	0.623 ± 0.003	5.81 ± 0.87	0.81	637.0 / 783
45	P011466112001	4.50 ± 0.11	0.092 ± 0.009	0.619 ± 0.003	5.79 ± 0.85	1.00	742.9 / 742
46	P011466112101	4.50 ± 0.09	0.091 ± 0.008	0.614 ± 0.003	5.79 ± 0.81	0.86	661.4 / 772
47	P011466112201	4.31 ± 0.08	0.114 ± 0.009	0.591 ± 0.003	6.21 ± 1.01	1.03	733.1 / 713
48	P011466112301	4.50 ± 0.10	0.136 ± 0.015	0.580 ± 0.005	6.36 ± 1.30	0.96	592.2 / 616
49	P011466112401	4.18 ± 0.09	0.085 ± 0.007	0.563 ± 0.003	6.25 ± 0.94	0.93	688.3 / 743
50	P011466112402	3.60 ± 0.12	0.049 ± 0.006	0.574 ± 0.004	5.94 ± 1.05	0.89	419.1 / 473
51	P011466112501	3.65 ± 0.06	0.056 ± 0.004	0.567 ± 0.002	6.04 ± 0.76	0.96	771.9 / 805
52	P011466112601	3.53 ± 0.06	0.047 ± 0.003	0.564 ± 0.002	5.98 ± 0.76	0.96	741.8 / 772
53	P011466112701	2.85 ± 0.04	0.030 ± 0.002	0.557 ± 0.002	6.00 ± 0.76	0.99	738.1 / 746
54	P011466112801	2.43 ± 0.03	0.033 ± 0.001	0.547 ± 0.002	6.11 ± 0.80	0.97	735.8 / 761
55	P011466108401	2.51 ± 0.01	0.186 ± 0.002	0.736 ± 0.002	5.38 ± 0.60	2.05	2151.0 / 1051
56	P011466108402	2.46 ± 0.01	0.174 ± 0.002	0.751 ± 0.002	5.16 ± 0.58	2.42	2512.2 / 1037
57	P011466108403	2.49 ± 0.01	0.174 ± 0.002	0.743 ± 0.003	5.32 ± 0.66	1.90	1879.9 / 992
58	P011466108501	2.46 ± 0.01	0.102 ± 0.002	0.730 ± 0.002	5.38 ± 0.58	2.10	2049.9 / 975
59	P011466112901	2.41 ± 0.01	0.100 ± 0.001	0.538 ± 0.002	6.02 ± 0.80	1.25	1229.2 / 981
60	P011466113001	2.33 ± 0.01	0.119 ± 0.001	0.525 ± 0.002	5.84 ± 0.88	1.22	1173.5 / 960
61	P011466113101	2.19 ± 0.01	0.182 ± 0.002	0.478 ± 0.003	5.91 ± 1.09	1.09	1105.3 / 1014

NOTE—In column 3-8, we show the following information: the dimensionless photon index of power-law  $\Gamma$ ; the scattered fraction  $f_{\text{sc}}$ ; the temperature of inner disk radius  $T_{\text{in}}$  in the unit of keV; the inner radius  $R_{\text{in}}$  of the thin accretion disk in the unit of gravitational radius; the reduced chi-square; the total chi-square  $\chi^2$  and degrees of freedom d.o.f..

**Table 3.** Best-fit parameters for spectra with the model CONSTANT\*TBABS\*SIMPL\*KERRBB2 ( $\alpha = 0.01$ ,  $M = 8.48 M_{\odot}$ ,  $i = 63^{\circ}$  and  $D = 2.96$  kpc)

Number	ObsID	SIMPL		KERRBB2		Reduced $\chi^2_{\nu}$	$\chi^2/\text{d.o.f.}$	$l^c$
		$\Gamma$	$f_{\text{sc}}$	$a_*^a$	$\dot{M}^b$			
1	P011466108502	2.24 ± 0.01	0.1016 ± 0.0022	0.129 ± 0.009	2.72 ± 0.03	1.22	1130.6 / 923	0.142
2	P011466108601	2.29 ± 0.02	0.0901 ± 0.0021	0.083 ± 0.011	2.94 ± 0.03	1.18	1090.7 / 921	0.150
3	P011466108602	2.15 ± 0.01	0.0956 ± 0.0019	0.116 ± 0.009	2.81 ± 0.03	1.10	974.1 / 887	0.146
4	P011466108702	2.17 ± 0.02	0.0573 ± 0.0017	0.096 ± 0.012	2.91 ± 0.03	1.10	917.5 / 835	0.149
5	P011466108801	2.15 ± 0.02	0.0472 ± 0.0012	0.076 ± 0.008	2.94 ± 0.02	1.06	1037.4 / 980	0.149
6	P011466108802	2.07 ± 0.02	0.0400 ± 0.0015	0.107 ± 0.007	2.85 ± 0.02	1.02	913.7 / 899	0.147
7	P011466108901	2.04 ± 0.02	0.0258 ± 0.0010	0.155 ± 0.007	2.62 ± 0.02	0.95	831.2 / 878	0.140
8	P011466109001	2.07 ± 0.02	0.0303 ± 0.0009	0.123 ± 0.005	2.75 ± 0.01	1.11	1106.3 / 993	0.143
9	P011466109101	2.18 ± 0.02	0.0437 ± 0.0015	0.072 ± 0.009	2.90 ± 0.02	0.95	855.1 / 903	0.146
10	P011466109102	2.06 ± 0.02	0.0344 ± 0.0011	0.109 ± 0.005	2.78 ± 0.02	0.98	907.1 / 923	0.144
11	P011466109201	2.07 ± 0.02	0.0324 ± 0.0011	0.124 ± 0.006	2.69 ± 0.02	0.99	892.5 / 901	0.141
12	P011466109202	2.08 ± 0.03	0.0304 ± 0.0012	0.127 ± 0.006	2.68 ± 0.02	1.00	922.0 / 921	0.140
13	P011466109301	2.04 ± 0.02	0.0246 ± 0.0009	0.126 ± 0.006	2.67 ± 0.02	1.03	911.4 / 888	0.139
14	P011466109401	2.06 ± 0.03	0.0205 ± 0.0009	0.139 ± 0.006	2.59 ± 0.02	1.01	908.1 / 896	0.136
15	P011466109501	2.14 ± 0.02	0.0236 ± 0.0009	0.128 ± 0.004	2.61 ± 0.01	0.98	991.3 / 1011	0.136
16	P011466109503	2.17 ± 0.03	0.0337 ± 0.0018	0.091 ± 0.012	2.74 ± 0.03	0.92	678.3 / 741	0.140
17	P011466109601	2.10 ± 0.02	0.0330 ± 0.0010	0.106 ± 0.005	2.67 ± 0.01	0.98	982.1 / 998	0.138
18	P011466109602	2.09 ± 0.02	0.0344 ± 0.0012	0.106 ± 0.006	2.66 ± 0.02	1.05	961.7 / 918	0.137
19	P011466109701	2.18 ± 0.02	0.0404 ± 0.0012	0.072 ± 0.008	2.70 ± 0.02	1.05	1002.3 / 957	0.136
20	P011466109702	2.18 ± 0.02	0.0378 ± 0.0012	0.074 ± 0.008	2.69 ± 0.02	1.06	1011.1 / 950	0.136
21	P011466109801	2.16 ± 0.03	0.0236 ± 0.0010	0.112 ± 0.005	2.53 ± 0.01	0.96	939.4 / 979	0.131
22	P011466109802	2.21 ± 0.03	0.0268 ± 0.0011	0.107 ± 0.005	2.54 ± 0.01	1.04	1015.6 / 976	0.131
23	P011466109803	2.24 ± 0.03	0.0247 ± 0.0012	0.115 ± 0.005	2.51 ± 0.01	1.01	966.9 / 960	0.130
24	P011466109901	2.22 ± 0.03	0.0194 ± 0.0010	0.108 ± 0.004	2.50 ± 0.01	0.92	894.6 / 971	0.129
25	P011466110001	2.50(f)	0.0139 ± 0.0002	0.139 ± 0.004	2.36 ± 0.01	0.88	834.1 / 943	0.124
26	P011466110101	2.50(f)	0.0127 ± 0.0002	0.151 ± 0.004	2.28 ± 0.01	0.90	835.7 / 924	0.121
27	P011466110201	2.50(f)	0.0118 ± 0.0002	0.158 ± 0.004	2.21 ± 0.01	0.91	897.9 / 984	0.118
28	P011466110301	2.50(f)	0.0110 ± 0.0002	0.161 ± 0.005	2.18 ± 0.01	0.90	821.7 / 911	0.116
29	P011466110302	2.50(f)	0.0112 ± 0.0002	0.152 ± 0.004	2.20 ± 0.01	0.97	903.3 / 934	0.117
30	P011466110401	2.50(f)	0.0127 ± 0.0002	0.207 ± 0.003	2.04 ± 0.01	1.10	1040.2 / 947	0.112
31	P011466110701	2.50(f)	0.0113 ± 0.0002	0.187 ± 0.005	2.04 ± 0.01	1.04	1037.0 / 995	0.111
32	P011466110801	2.50(f)	0.0103 ± 0.0003	0.176 ± 0.006	2.05 ± 0.01	1.02	901.4 / 888	0.110
33	P011466110901	2.50(f)	0.0112 ± 0.0002	0.217 ± 0.003	1.89 ± 0.01	1.13	1064.2 / 945	0.104
34	P011466110902	2.50(f)	0.0121 ± 0.0004	0.218 ± 0.004	1.88 ± 0.01	0.90	716.3 / 800	0.104
35	P011466111001	2.50(f)	0.0146 ± 0.0003	0.223 ± 0.003	1.85 ± 0.01	1.13	1067.2 / 945	0.103
36	P011466111201	2.50(f)	0.0125 ± 0.0003	0.237 ± 0.004	1.75 ± 0.01	1.04	936.2 / 903	0.098
37	P011466111301	2.50(f)	0.0116 ± 0.0003	0.232 ± 0.004	1.74 ± 0.01	1.00	880.5 / 880	0.097
38	P011466111401	2.50(f)	0.0090 ± 0.0003	0.227 ± 0.003	1.69 ± 0.01	1.15	1034.1 / 900	0.094
39	P011466111501	2.50(f)	0.0105 ± 0.0003	0.242 ± 0.004	1.61 ± 0.01	1.26	1124.4 / 895	0.091
40	P011466111601	2.50(f)	0.0127 ± 0.0003	0.234 ± 0.004	1.57 ± 0.01	1.04	874.8 / 838	0.088
41	P011466111701	2.50(f)	0.0118 ± 0.0003	0.223 ± 0.004	1.54 ± 0.01	1.04	860.1 / 827	0.086
42	P011466111801	2.50(f)	0.0200 ± 0.0007	0.231 ± 0.007	1.47 ± 0.01	1.07	587.7 / 550	0.082
43	P011466111802	2.50(f)	0.0196 ± 0.0009	0.253 ± 0.014	1.41 ± 0.03	1.21	522.8 / 433	0.080
44	P011466111901	2.50(f)	0.0135 ± 0.0004	0.227 ± 0.006	1.41 ± 0.01	1.01	818.5 / 811	0.079
45	P011466112001	2.50(f)	0.0132 ± 0.0005	0.230 ± 0.005	1.37 ± 0.01	1.24	948.5 / 768	0.076
46	P011466112101	2.50(f)	0.0135 ± 0.0004	0.228 ± 0.005	1.32 ± 0.01	1.14	912.0 / 801	0.074
47	P011466112201	2.50(f)	0.0194 ± 0.0005	0.216 ± 0.006	1.30 ± 0.01	1.35	990.2 / 731	0.072
48	P011466112301	2.50(f)	0.0171 ± 0.0005	0.227 ± 0.009	1.24 ± 0.02	1.34	846.4 / 632	0.069
49	P011466112401	2.50(f)	0.0199 ± 0.0005	0.156 ± 0.009	1.15 ± 0.01	1.26	974.8 / 772	0.061
50	P011466112402	2.50(f)	0.0209 ± 0.0008	0.156 ± 0.015	1.14 ± 0.02	0.94	455.9 / 484	0.061
51	P011466112501	2.50(f)	0.0241 ± 0.0004	0.141 ± 0.007	1.14 ± 0.01	1.30	1095.5 / 843	0.060
52	P011466112601	2.50(f)	0.0227 ± 0.0004	0.149 ± 0.007	1.09 ± 0.01	1.16	933.6 / 804	0.058
53	P011466112701	2.63 ± 0.04	0.0389 ± 0.0023	0.047 ± 0.014	1.15 ± 0.02	1.05	815.0 / 773	0.057
54	P011466112801	2.32 ± 0.03	0.0491 ± 0.0019	0.016 ± 0.013	1.14 ± 0.02	0.98	771.3 / 791	0.056
55	P011466108401	2.36 ± 0.01	0.2537 ± 0.0024	0.133 ± 0.009	2.83 ± 0.03	1.64	1850.6 / 1125	0.149
56	P011466108402	2.34 ± 0.01	0.2521 ± 0.0024	0.153 ± 0.010	2.79 ± 0.03	1.68	1864.5 / 1108	0.148
57	P011466108403	2.39 ± 0.01	0.2589 ± 0.0029	0.073 ± 0.014	3.02 ± 0.04	1.35	1412.7 / 1044	0.153
58	P011466108501	2.31 ± 0.01	0.1479 ± 0.0022	0.121 ± 0.008	2.63 ± 0.02	1.50	1540.6 / 1024	0.137
59	P011466112901	2.36 ± 0.01	0.1573 ± 0.0018	0.035 ± 0.015	1.07 ± 0.02	1.24	1292.8 / 1044	0.053
60	P011466113001	2.29 ± 0.01	0.1875 ± 0.0020	0.109 ± 0.013	0.88 ± 0.01	1.18	1196.2 / 1013	0.046
61	P011466113101	2.16 ± 0.01	0.2778 ± 0.0021	0.200 ± 0.022	0.60 ± 0.02	1.09	1183.6 / 1087	0.033

NOTE—<sup>a</sup> the dimensionless spin parameter  $a_*$ .<sup>b</sup> the mass accretion rate  $\dot{M}$  in units of  $10^{18} \text{ g s}^{-1}$ .<sup>c</sup> the bolometric Eddington-scaled luminosity  $l = L(a_*, \dot{M})/L_{\text{Edd}}$ .

**Table 4.** Best-fit parameters for spectra with the model CONSTANT\*TBABS\*SIMPL\*KERRBB2 ( $\alpha = 0.1$ ,  $M = 8.48 M_{\odot}$ ,  $i = 63^{\circ}$  and  $D = 2.96$  kpc)

Number	ObsID	SIMPL		KERRBB2		Reduced $\chi^2_{\nu}$	$\chi^2/\text{d.o.f.}$	$l$
		$\Gamma$	$f_{\text{sc}}$	$a_*^a$	$\dot{M}^b$			
1	P011466108502	2.25 ± 0.01	0.1030 ± 0.0021	0.059 ± 0.011	2.86 ± 0.03	1.22	1129.4 / 923	0.143
2	P011466108601	2.27 ± 0.02	0.0882 ± 0.0022	0.029 ± 0.010	3.04 ± 0.03	1.18	1087.8 / 921	0.150
3	P011466108602	2.15 ± 0.01	0.0963 ± 0.0019	0.046 ± 0.011	2.94 ± 0.03	1.10	974.6 / 887	0.146
4	P011466108702	2.16 ± 0.02	0.0563 ± 0.0018	0.036 ± 0.010	3.01 ± 0.03	1.09	914.4 / 835	0.149
5	P011466108801	2.14 ± 0.02	0.0465 ± 0.0013	0.019 ± 0.006	3.04 ± 0.02	1.06	1037.5 / 980	0.149
6	P011466108802	2.07 ± 0.02	0.0405 ± 0.0014	0.036 ± 0.008	2.99 ± 0.02	1.01	910.4 / 899	0.148
7	P011466108901	2.05 ± 0.02	0.0265 ± 0.0010	0.098 ± 0.009	2.73 ± 0.02	0.95	836.0 / 878	0.140
8	P011466109001	2.08 ± 0.02	0.0309 ± 0.0008	0.055 ± 0.006	2.88 ± 0.02	1.11	1105.2 / 993	0.144
9	P011466109101	2.17 ± 0.02	0.0430 ± 0.0016	0.015 ± 0.007	2.99 ± 0.02	0.95	856.6 / 903	0.146
10	P011466109102	2.07 ± 0.02	0.0348 ± 0.0011	0.039 ± 0.007	2.91 ± 0.02	0.98	904.8 / 923	0.144
11	P011466109201	2.08 ± 0.02	0.0330 ± 0.0011	0.058 ± 0.007	2.82 ± 0.02	0.99	891.9 / 901	0.141
12	P011466109202	2.09 ± 0.03	0.0311 ± 0.0012	0.062 ± 0.007	2.80 ± 0.02	1.00	922.6 / 921	0.141
13	P011466109301	2.05 ± 0.02	0.0251 ± 0.0009	0.061 ± 0.007	2.79 ± 0.02	1.03	913.6 / 888	0.140
14	P011466109401	2.07 ± 0.03	0.0212 ± 0.0008	0.077 ± 0.007	2.70 ± 0.02	1.02	911.8 / 896	0.137
15	P011466109501	2.15 ± 0.02	0.0242 ± 0.0008	0.065 ± 0.006	2.72 ± 0.01	0.98	992.3 / 1011	0.137
16	P011466109503	2.15 ± 0.04	0.0331 ± 0.0019	0.031 ± 0.010	2.84 ± 0.03	0.91	677.4 / 741	0.140
17	P011466109601	2.10 ± 0.02	0.0333 ± 0.0009	0.037 ± 0.006	2.79 ± 0.02	0.98	976.5 / 998	0.138
18	P011466109602	2.10 ± 0.02	0.0348 ± 0.0012	0.037 ± 0.007	2.78 ± 0.02	1.04	957.4 / 918	0.138
19	P011466109701	2.17 ± 0.02	0.0397 ± 0.0012	0.018 ± 0.006	2.79 ± 0.02	1.05	1001.2 / 957	0.136
20	P011466109702	2.16 ± 0.02	0.0372 ± 0.0012	0.020 ± 0.006	2.77 ± 0.02	1.06	1010.0 / 950	0.136
21	P011466109801	2.17 ± 0.03	0.0240 ± 0.0010	0.046 ± 0.006	2.64 ± 0.01	0.96	935.9 / 979	0.132
22	P011466109802	2.22 ± 0.02	0.0271 ± 0.0010	0.040 ± 0.006	2.65 ± 0.01	1.03	1009.8 / 976	0.131
23	P011466109803	2.25 ± 0.03	0.0251 ± 0.0011	0.050 ± 0.006	2.63 ± 0.02	1.00	964.1 / 960	0.131
24	P011466109901	2.23 ± 0.03	0.0196 ± 0.0009	0.042 ± 0.005	2.62 ± 0.01	0.92	890.3 / 971	0.130
25	P011466110001	2.50(f)	0.0141 ± 0.0002	0.083 ± 0.005	2.45 ± 0.01	0.89	838.4 / 943	0.125
26	P011466110101	2.50(f)	0.0129 ± 0.0002	0.102 ± 0.003	2.35 ± 0.01	0.91	839.5 / 924	0.121
27	P011466110201	2.50(f)	0.0119 ± 0.0002	0.109 ± 0.003	2.28 ± 0.01	0.92	901.7 / 984	0.118
28	P011466110301	2.50(f)	0.0111 ± 0.0002	0.111 ± 0.003	2.25 ± 0.01	0.90	823.5 / 911	0.116
29	P011466110302	2.50(f)	0.0113 ± 0.0003	0.105 ± 0.003	2.27 ± 0.01	0.97	909.2 / 934	0.117
30	P011466110401	2.50(f)	0.0129 ± 0.0002	0.142 ± 0.004	2.14 ± 0.01	1.08	1026.1 / 947	0.113
31	P011466110701	2.50(f)	0.0113 ± 0.0002	0.132 ± 0.003	2.12 ± 0.01	1.02	1018.1 / 995	0.111
32	P011466110801	2.50(f)	0.0103 ± 0.0003	0.124 ± 0.004	2.12 ± 0.01	1.01	897.7 / 888	0.110
33	P011466110901	2.50(f)	0.0115 ± 0.0002	0.156 ± 0.004	1.98 ± 0.01	1.11	1053.4 / 945	0.105
34	P011466110902	2.50(f)	0.0124 ± 0.0004	0.160 ± 0.006	1.97 ± 0.01	0.89	714.5 / 800	0.105
35	P011466111001	2.50(f)	0.0150 ± 0.0003	0.164 ± 0.004	1.94 ± 0.01	1.12	1057.4 / 945	0.104
36	P011466111201	2.50(f)	0.0129 ± 0.0003	0.186 ± 0.005	1.82 ± 0.01	1.04	941.3 / 903	0.099
37	P011466111301	2.50(f)	0.0120 ± 0.0003	0.177 ± 0.005	1.81 ± 0.01	1.00	882.2 / 880	0.098
38	P011466111401	2.50(f)	0.0093 ± 0.0003	0.171 ± 0.005	1.76 ± 0.01	1.15	1030.6 / 900	0.095
39	P011466111501	2.50(f)	0.0107 ± 0.0003	0.206 ± 0.003	1.65 ± 0.01	1.26	1131.8 / 895	0.091
40	P011466111601	2.50(f)	0.0131 ± 0.0003	0.180 ± 0.007	1.63 ± 0.01	1.04	874.2 / 838	0.088
41	P011466111701	2.50(f)	0.0121 ± 0.0003	0.167 ± 0.006	1.60 ± 0.01	1.04	856.9 / 827	0.086
42	P011466111801	2.50(f)	0.0206 ± 0.0007	0.177 ± 0.011	1.53 ± 0.02	1.06	584.7 / 550	0.083
43	P011466111802	2.50(f)	0.0200 ± 0.0009	0.216 ± 0.012	1.44 ± 0.02	1.20	520.3 / 433	0.080
44	P011466111901	2.50(f)	0.0140 ± 0.0004	0.170 ± 0.009	1.48 ± 0.01	1.00	810.4 / 811	0.079
45	P011466112001	2.50(f)	0.0138 ± 0.0004	0.176 ± 0.008	1.43 ± 0.01	1.23	942.1 / 768	0.077
46	P011466112101	2.50(f)	0.0141 ± 0.0004	0.172 ± 0.008	1.38 ± 0.01	1.13	904.0 / 801	0.074
47	P011466112201	2.50(f)	0.0215 ± 0.0005	0.145 ± 0.008	1.38 ± 0.01	1.44	1055.0 / 734	0.073
48	P011466112301	2.50(f)	0.0178 ± 0.0006	0.166 ± 0.014	1.31 ± 0.02	1.33	837.6 / 632	0.070
49	P011466112401	2.50(f)	0.0203 ± 0.0005	0.114 ± 0.007	1.18 ± 0.01	1.24	954.9 / 772	0.061
50	P011466112402	2.50(f)	0.0214 ± 0.0008	0.111 ± 0.011	1.17 ± 0.02	0.93	450.5 / 484	0.061
51	P011466112501	2.50(f)	0.0248 ± 0.0004	0.083 ± 0.009	1.18 ± 0.01	1.26	1062.1 / 843	0.060
52	P011466112601	2.50(f)	0.0234 ± 0.0004	0.092 ± 0.010	1.13 ± 0.01	1.14	914.8 / 804	0.058
53	P011466112701	2.59 ± 0.04	0.0377 ± 0.0020	-0.001 ± 0.015	1.18 ± 0.02	1.05	809.4 / 773	0.057
54	P011466112801	2.30 ± 0.02	0.0480 ± 0.0016	-0.038 ± 0.014	1.18 ± 0.02	0.97	766.4 / 791	0.056
55	P011466108401	2.36 ± 0.01	0.2556 ± 0.0023	0.058 ± 0.011	2.99 ± 0.03	1.64	1847.8 / 1125	0.150
56	P011466108402	2.35 ± 0.01	0.2547 ± 0.0023	0.079 ± 0.012	2.94 ± 0.03	1.68	1862.2 / 1108	0.149
57	P011466108403	2.38 ± 0.01	0.2551 ± 0.0031	0.028 ± 0.013	3.09 ± 0.03	1.35	1404.4 / 1044	0.152
58	P011466108501	2.32 ± 0.01	0.1497 ± 0.0021	0.047 ± 0.010	2.77 ± 0.02	1.49	1530.4 / 1024	0.138
59	P011466112901	2.34 ± 0.01	0.1541 ± 0.0016	-0.010 ± 0.016	1.09 ± 0.02	1.21	1258.2 / 1044	0.053
60	P011466113001	2.27 ± 0.01	0.1841 ± 0.0018	0.041 ± 0.016	0.92 ± 0.02	1.15	1165.5 / 1013	0.046
61	P011466113101	2.16 ± 0.00	0.2747 ± 0.0022	0.058 ± 0.024	0.68 ± 0.02	1.08	1172.2 / 1087	0.034

**Table 5.** Best-fit parameters for spectra with the model CONSTANT\*TBABS\*SIMPL\*KERRBB2 ( $\alpha = 0.01$ ,  $M = 8.06 M_{\odot}$ ,  $i = 66^{\circ}.2$  and  $D = 2.96$  kpc)

Number	ObsID	SIMPL		KERRBB2		Reduced $\chi^2_{\nu}$	$\chi^2/\text{d.o.f.}$	$l$
		$\Gamma$	$f_{\text{sc}}$	$a_*^a$	$\dot{M}^b$			
1	P011466108502	2.25 ± 0.01	0.1046 ± 0.0021	-0.129 ± 0.013	3.63 ± 0.04	1.23	1137.9 / 923	0.173
2	P011466108601	2.28 ± 0.02	0.0897 ± 0.0022	-0.163 ± 0.011	3.86 ± 0.04	1.19	1093.1 / 921	0.181
3	P011466108602	2.16 ± 0.01	0.0974 ± 0.0019	-0.141 ± 0.012	3.73 ± 0.04	1.10	979.3 / 887	0.177
4	P011466108702	2.16 ± 0.02	0.0572 ± 0.0018	-0.152 ± 0.011	3.82 ± 0.04	1.10	918.3 / 835	0.180
5	P011466108801	2.15 ± 0.02	0.0474 ± 0.0013	-0.172 ± 0.007	3.86 ± 0.02	1.06	1043.0 / 980	0.180
6	P011466108802	2.08 ± 0.02	0.0415 ± 0.0015	-0.153 ± 0.009	3.79 ± 0.03	1.02	916.9 / 899	0.178
7	P011466108901	2.04 ± 0.02	0.0262 ± 0.0010	-0.079 ± 0.007	3.45 ± 0.02	0.95	836.3 / 878	0.168
8	P011466109001	2.09 ± 0.02	0.0318 ± 0.0009	-0.129 ± 0.007	3.65 ± 0.02	1.12	1116.2 / 993	0.174
9	P011466109101	2.17 ± 0.02	0.0439 ± 0.0016	-0.177 ± 0.009	3.80 ± 0.03	0.95	861.1 / 903	0.177
10	P011466109102	2.08 ± 0.02	0.0355 ± 0.0011	-0.148 ± 0.008	3.69 ± 0.02	0.99	912.2 / 923	0.174
11	P011466109201	2.09 ± 0.02	0.0339 ± 0.0011	-0.126 ± 0.009	3.57 ± 0.03	1.00	898.7 / 901	0.170
12	P011466109202	2.10 ± 0.02	0.0320 ± 0.0012	-0.122 ± 0.009	3.55 ± 0.03	1.01	929.1 / 921	0.170
13	P011466109301	2.06 ± 0.02	0.0257 ± 0.0009	-0.122 ± 0.008	3.53 ± 0.02	1.04	921.4 / 888	0.169
14	P011466109401	2.06 ± 0.03	0.0211 ± 0.0009	-0.095 ± 0.006	3.39 ± 0.02	1.02	918.1 / 896	0.164
15	P011466109501	2.17 ± 0.02	0.0250 ± 0.0008	-0.118 ± 0.007	3.45 ± 0.02	0.99	1002.1 / 1011	0.165
16	P011466109503	2.16 ± 0.04	0.0338 ± 0.0019	-0.159 ± 0.012	3.60 ± 0.04	0.92	679.1 / 741	0.169
17	P011466109601	2.11 ± 0.02	0.0341 ± 0.0009	-0.152 ± 0.007	3.54 ± 0.02	0.99	985.2 / 998	0.167
18	P011466109602	2.11 ± 0.02	0.0356 ± 0.0012	-0.153 ± 0.008	3.53 ± 0.02	1.05	963.9 / 918	0.166
19	P011466109701	2.18 ± 0.02	0.0405 ± 0.0012	-0.176 ± 0.007	3.54 ± 0.02	1.05	1006.0 / 957	0.165
20	P011466109702	2.17 ± 0.02	0.0379 ± 0.0012	-0.174 ± 0.007	3.52 ± 0.02	1.07	1015.4 / 950	0.164
21	P011466109801	2.18 ± 0.03	0.0247 ± 0.0010	-0.142 ± 0.007	3.35 ± 0.02	0.96	942.4 / 979	0.159
22	P011466109802	2.23 ± 0.02	0.0278 ± 0.0010	-0.150 ± 0.007	3.36 ± 0.02	1.04	1016.6 / 976	0.158
23	P011466109803	2.26 ± 0.03	0.0260 ± 0.0012	-0.138 ± 0.008	3.33 ± 0.02	1.01	970.1 / 960	0.158
24	P011466109901	2.24 ± 0.03	0.0203 ± 0.0009	-0.146 ± 0.007	3.32 ± 0.02	0.92	893.8 / 971	0.156
25	P011466110001	2.50(f)	0.0142 ± 0.0002	-0.093 ± 0.004	3.09 ± 0.01	0.90	844.1 / 943	0.150
26	P011466110101	2.50(f)	0.0129 ± 0.0002	-0.082 ± 0.004	2.99 ± 0.01	0.91	838.6 / 924	0.146
27	P011466110201	2.50(f)	0.0120 ± 0.0002	-0.073 ± 0.004	2.90 ± 0.01	0.92	904.2 / 984	0.142
28	P011466110301	2.50(f)	0.0112 ± 0.0002	-0.071 ± 0.004	2.86 ± 0.01	0.90	824.4 / 911	0.140
29	P011466110302	2.50(f)	0.0114 ± 0.0003	-0.079 ± 0.004	2.88 ± 0.01	0.97	909.7 / 934	0.141
30	P011466110401	2.50(f)	0.0130 ± 0.0002	-0.031 ± 0.005	2.71 ± 0.01	1.10	1040.3 / 947	0.136
31	P011466110701	2.50(f)	0.0114 ± 0.0002	-0.044 ± 0.004	2.69 ± 0.01	1.04	1032.8 / 995	0.134
32	P011466110801	2.50(f)	0.0104 ± 0.0003	-0.055 ± 0.005	2.69 ± 0.01	1.02	902.7 / 888	0.133
33	P011466110901	2.50(f)	0.0116 ± 0.0002	-0.013 ± 0.006	2.50 ± 0.01	1.14	1078.3 / 945	0.127
34	P011466110902	2.50(f)	0.0125 ± 0.0004	-0.007 ± 0.008	2.48 ± 0.02	0.90	721.1 / 800	0.126
35	P011466111001	2.50(f)	0.0149 ± 0.0003	0.008 ± 0.003	2.42 ± 0.01	1.15	1082.7 / 945	0.124
36	P011466111201	2.50(f)	0.0127 ± 0.0003	0.024 ± 0.004	2.28 ± 0.01	1.05	944.2 / 903	0.118
37	P011466111301	2.50(f)	0.0118 ± 0.0003	0.017 ± 0.004	2.27 ± 0.01	1.01	890.4 / 880	0.117
38	P011466111401	2.50(f)	0.0092 ± 0.0003	0.011 ± 0.004	2.20 ± 0.01	1.16	1045.7 / 900	0.113
39	P011466111501	2.50(f)	0.0108 ± 0.0003	0.028 ± 0.004	2.11 ± 0.01	1.26	1131.7 / 895	0.109
40	P011466111601	2.50(f)	0.0130 ± 0.0003	0.016 ± 0.005	2.05 ± 0.01	1.05	880.8 / 838	0.106
41	P011466111701	2.50(f)	0.0123 ± 0.0003	-0.008 ± 0.008	2.04 ± 0.02	1.04	863.2 / 827	0.103
42	P011466111801	2.50(f)	0.0205 ± 0.0007	0.010 ± 0.009	1.93 ± 0.02	1.07	587.4 / 550	0.099
43	P011466111802	2.50(f)	0.0201 ± 0.0009	0.036 ± 0.017	1.85 ± 0.03	1.20	521.4 / 433	0.096
44	P011466111901	2.50(f)	0.0139 ± 0.0004	0.008 ± 0.007	1.85 ± 0.01	1.01	818.5 / 811	0.095
45	P011466112001	2.50(f)	0.0136 ± 0.0005	0.011 ± 0.006	1.79 ± 0.01	1.24	948.8 / 768	0.092
46	P011466112101	2.50(f)	0.0139 ± 0.0004	0.009 ± 0.006	1.73 ± 0.01	1.14	914.8 / 801	0.089
47	P011466112201	2.50(f)	0.0215 ± 0.0005	-0.042 ± 0.011	1.76 ± 0.02	1.45	1064.9 / 734	0.088
48	P011466112301	2.50(f)	0.0178 ± 0.0006	-0.016 ± 0.019	1.67 ± 0.03	1.34	844.2 / 632	0.084
49	P011466112401	2.50(f)	0.0202 ± 0.0005	-0.080 ± 0.008	1.51 ± 0.01	1.25	966.9 / 772	0.074
50	P011466112402	2.50(f)	0.0213 ± 0.0008	-0.083 ± 0.014	1.50 ± 0.02	0.94	453.8 / 484	0.073
51	P011466112501	2.50(f)	0.0247 ± 0.0004	-0.113 ± 0.011	1.51 ± 0.01	1.29	1083.6 / 843	0.072
52	P011466112601	2.50(f)	0.0230 ± 0.0004	-0.092 ± 0.007	1.42 ± 0.01	1.16	929.8 / 804	0.069
53	P011466112701	2.63 ± 0.04	0.0392 ± 0.0022	-0.232 ± 0.018	1.53 ± 0.02	1.05	812.1 / 773	0.069
54	P011466112801	2.32 ± 0.03	0.0495 ± 0.0018	-0.276 ± 0.016	1.52 ± 0.02	0.97	769.5 / 791	0.067
55	P011466108401	2.36 ± 0.01	0.2581 ± 0.0022	-0.134 ± 0.012	3.81 ± 0.04	1.66	1864.2 / 1125	0.181
56	P011466108402	2.34 ± 0.01	0.2523 ± 0.0024	-0.080 ± 0.011	3.67 ± 0.03	1.69	1877.8 / 1108	0.179
57	P011466108403	2.38 ± 0.01	0.2578 ± 0.0031	-0.170 ± 0.015	3.96 ± 0.04	1.35	1411.2 / 1044	0.185
58	P011466108501	2.32 ± 0.01	0.1518 ± 0.0021	-0.146 ± 0.012	3.53 ± 0.03	1.51	1542.9 / 1024	0.167
59	P011466112901	2.36 ± 0.01	0.1588 ± 0.0018	-0.265 ± 0.018	1.43 ± 0.02	1.24	1290.7 / 1044	0.064
60	P011466113001	2.29 ± 0.01	0.1884 ± 0.0020	-0.167 ± 0.022	1.18 ± 0.02	1.18	1194.8 / 1013	0.055
61	P011466113101	2.17 ± 0.01	0.2802 ± 0.0022	-0.146 ± 0.035	0.87 ± 0.03	1.09	1189.3 / 1087	0.041

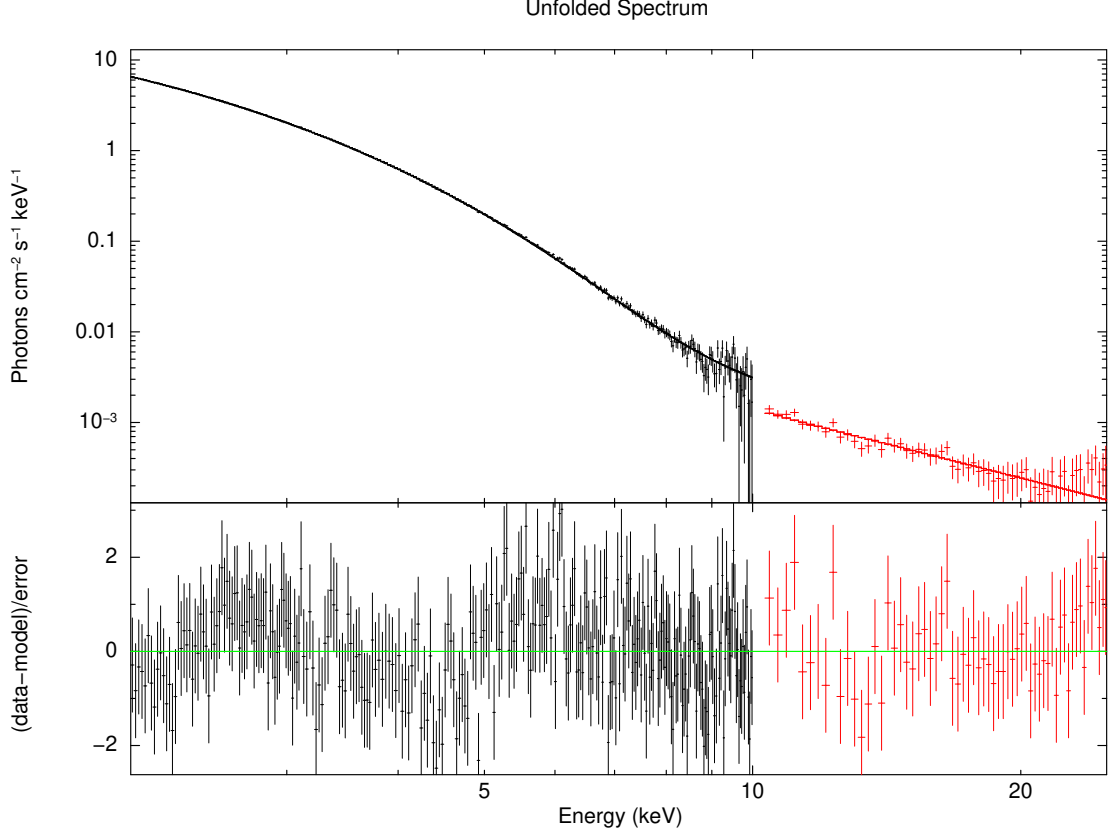


**Figure 2.** A representative (ObsID P011466110701) unfolded spectrum. The spectrum was rebinned just for the purpose of display.

**Table 6.** Effect of Different  $\Gamma$  and CONSTANT normalization (only for P011466110701, where  $\alpha = 0.01$ ,  $M = 8.48 M_{\odot}$ ,  $i = 63^{\circ}$  and  $D = 2.96$  kpc)

N	Model	Parameter	Case 1	Case 2	Case 3	Case 4	Case 5	Case 6	Case 7
1	SIMPL	$\Gamma$	2.10(f)	2.30(f)	2.50(f)	2.50(f)	2.50(f)	2.70(f)	2.90(f)
2	SIMPL	$f_{sc}$	$0.0058 \pm 0.0001$	$0.0081 \pm 0.0002$	$0.0113 \pm 0.0002$	$0.0108 \pm 0.0002$	$0.0101 \pm 0.0002$	$0.0152 \pm 0.0003$	$0.0201 \pm 0.0004$
3	KERRBB2	$a_*$	$0.213 \pm 0.002$	$0.207 \pm 0.002$	$0.187 \pm 0.005$	$0.190 \pm 0.005$	$0.204 \pm 0.002$	$0.174 \pm 0.004$	$0.160 \pm 0.004$
4	KERRBB2	$\dot{M}$	$1.99 \pm 0.01$	$2.00 \pm 0.01$	$2.04 \pm 0.01$	$2.04 \pm 0.01$	$2.01 \pm 0.01$	$2.07 \pm 0.01$	$2.10 \pm 0.01$
5	CONSTANT	norm	0.95(f)	0.95(f)	0.95(f)	1.00(f)	1.05(f)	0.95(f)	0.95(f)
6		Reduced $\chi^2_{\nu}$	1.21	1.12	1.04	1.07	1.11	0.97	0.91
7		$\chi^2/\text{d.o.f.}$	1201.1 / 995	1118.3 / 995	1037.0 / 995	1069.5 / 995	1100.6 / 995	963.5 / 995	908.6 / 995
8		$l$	0.110	0.110	0.111	0.111	0.110	0.112	0.112

## REFERENCES

- Abbott, R., Abbott, T. D., Abraham, S., & et al. 2020, arXiv e-prints, arXiv:2010.14527.  
<https://arxiv.org/abs/2010.14527>
- Atri, P., Miller-Jones, J. C. A., Bahramian, A., et al. 2020, MNRAS, 493, L81, doi: [10.1093/mnras/slaa010](https://doi.org/10.1093/mnras/slaa010)
- Bambi, C., & Barausse, E. 2011, ApJ, 731, 121, doi: [10.1088/0004-637X/731/2/121](https://doi.org/10.1088/0004-637X/731/2/121)
- Bambi, C., & Modesto, L. 2013, Physics Letters B, 721, 329, doi: <https://doi.org/10.1016/j.physletb.2013.03.025>
- Bardeen, J. M., Press, W. H., & Teukolsky, S. A. 1972, ApJ, 178, 347, doi: [10.1086/151796](https://doi.org/10.1086/151796)
- Bharali, P., Chauhan, J., & Boruah, K. 2019, MNRAS, 487, 5946, doi: [10.1093/mnras/stz1686](https://doi.org/10.1093/mnras/stz1686)
- Blandford, R. D., & Znajek, R. L. 1977, MNRAS, 179, 433, doi: [10.1093/mnras/179.3.433](https://doi.org/10.1093/mnras/179.3.433)

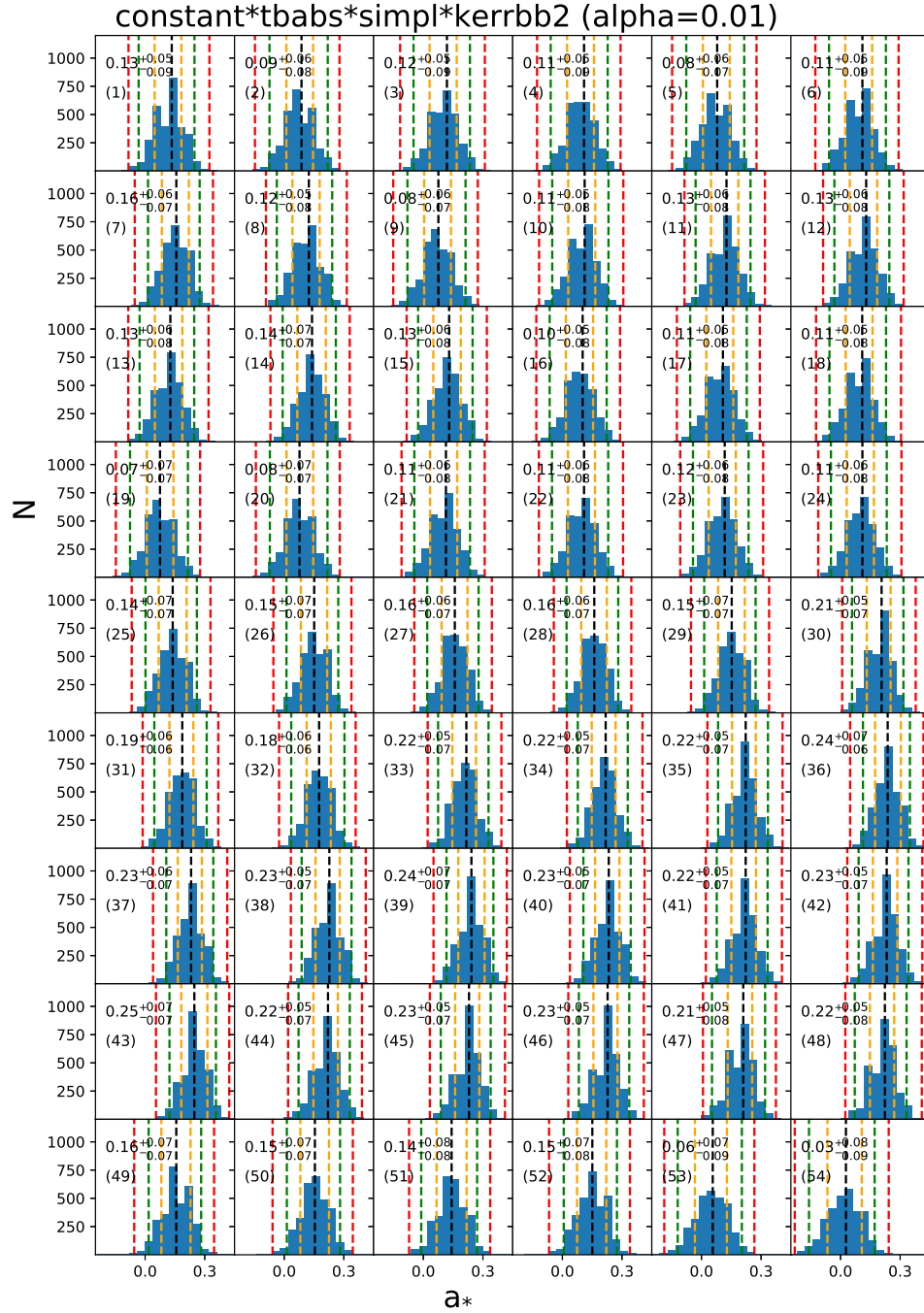


**Figure 3.** Histograms of  $a_*$  calculated via the Monte Carlo analysis for 3000 sets of parameters per spectrum. The three dashed lines imply the 99.7% ( $3\sigma$ , red), 95.4% ( $2\sigma$ , green), and 68.3% ( $1\sigma$ , orange) error, respectively. The respective 68.3% confidence level on  $a_*$  is indicated in each panel.

Buisson, D. J. K., Fabian, A. C., Barret, D., et al. 2019,

MNRAS, 490, 1350, doi: [10.1093/mnras/stz2681](https://doi.org/10.1093/mnras/stz2681)

Cao, X. L., Jiang, W. C., Meng, B., et al. 2020, Sci.

China-Phys. Mech. Astron, 63(4): 249504.

<https://arxiv.org/abs/1910.04451>

Chen, Y., Cui, W. W., Li, W., et al. 2020, Sci. China-Phys.

Mech. Astron, 63(4): 249505,

doi: [10.1007/s11433-019-1469-5](https://doi.org/10.1007/s11433-019-1469-5)

Chen, Z. H., Gou, L. J., McClintock, J. E., et al. 2016,

ApJ, 825, 45, doi: [10.3847/0004-637X/825/1/45](https://doi.org/10.3847/0004-637X/825/1/45)

Davis, S. W., Blaes, O. M., Hubeny, I., & Turner, N. J.

2005, ApJ, 621, 372, doi: [10.1086/427278](https://doi.org/10.1086/427278)



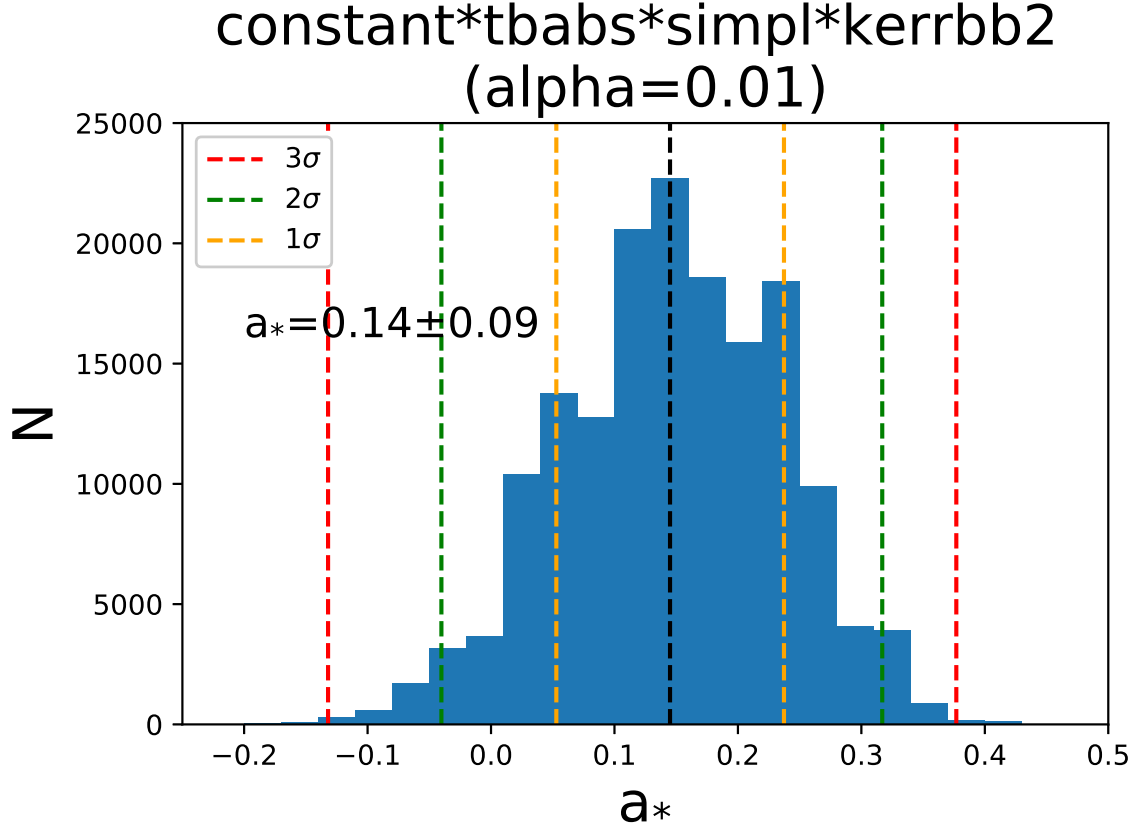


**Figure 4.** Summed histogram of  $a_*$  for 54 spectra, including 162000 data points.

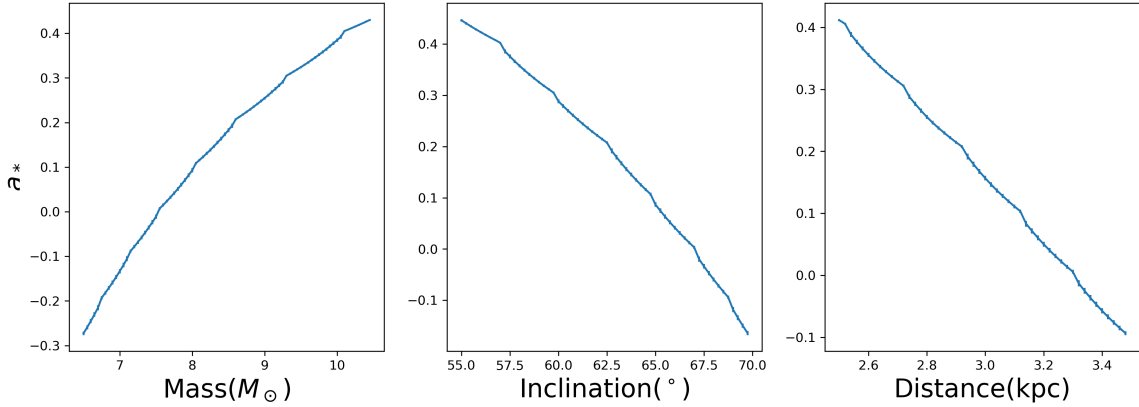


**Figure 5.** The correlation plots displaying the effect on the spin of varying  $M$ ,  $i$  and  $D$ .

Event Horizon Telescope Collaboration, Akiyama, K., Alberdi, A., et al. 2019, ApJL, 875, L1, doi: [10.3847/2041-8213/ab0ec7](https://doi.org/10.3847/2041-8213/ab0ec7)

Fabian, A. C., Rees, M. J., Stella, L., & White, N. E. 1989, MNRAS, 238, 729, doi: [10.1093/mnras/238.3.729](https://doi.org/10.1093/mnras/238.3.729)

Fabian, A. C., Buisson, D. J., Kosec, P., et al. 2020, MNRAS, 493, 5389, doi: [10.1093/mnras/staa564](https://doi.org/10.1093/mnras/staa564)

Fragos, T., Tremmel, M., Rantsiou, E., & Belczynski, K. 2010, ApJL, 719, L79, doi: [10.1088/2041-8205/719/1/L79](https://doi.org/10.1088/2041-8205/719/1/L79)

Gandhi, P., Rao, A., Johnson, M. A. C., Paice, J. A., & Maccarone, T. J. 2019, Monthly Notices of the Royal Astronomical Society, 485, 2642, doi: [10.1093/mnras/stz438](https://doi.org/10.1093/mnras/stz438)

- Gou, L., McClintock, J. E., Steiner, J. F., et al. 2010, *The Astrophysical Journal*, 718, L122, doi: [10.1088/2041-8205/718/2/1122](https://doi.org/10.1088/2041-8205/718/2/1122)
- Gou, L. J., McClintock, J. E., Liu, J. F., et al. 2009, *ApJ*, 701, 1076, doi: [10.1088/0004-637X/701/2/1076](https://doi.org/10.1088/0004-637X/701/2/1076)
- Gou, L. J., McClintock, J. E., Remillard, R. A., et al. 2014, *ApJ*, 790, 29, doi: [10.1088/0004-637X/790/1/29](https://doi.org/10.1088/0004-637X/790/1/29)
- Guo, C.-C., Liao, J.-Y., Zhang, S., et al. 2020, *Journal of High Energy Astrophysics*, 27, 44, doi: [10.1016/j.jheap.2020.02.008](https://doi.org/10.1016/j.jheap.2020.02.008)
- Kara, E., Steiner, J. F., Fabian, A. C., et al. 2019, *Nature*, 565, 198, doi: [10.1038/s41586-018-0803-x](https://doi.org/10.1038/s41586-018-0803-x)
- Kawamuro, T., Negoro, H., Yoneyama, T., et al. 2018, *The Astronomer's Telegram*, 11399, 1
- Kubota, A., Tanaka, Y., Makishima, K., et al. 1998, *PASJ*, 50, 667, doi: [10.1093/pasj/50.6.667](https://doi.org/10.1093/pasj/50.6.667)
- Kulkarni, A. K., Penna, R. F., Shcherbakov, R. V., et al. 2011, *MNRAS*, 414, 1183, doi: [10.1111/j.1365-2966.2011.18446.x](https://doi.org/10.1111/j.1365-2966.2011.18446.x)
- Li, L. X., Zimmerman, E. R., Narayan, R., & McClintock, J. E. 2005, *ApJS*, 157, 335, doi: [10.1086/428089](https://doi.org/10.1086/428089)
- Li, X., Li, X., Tan, Y., et al. 2020, *Journal of High Energy Astrophysics*, 27, 64, doi: [10.1016/j.jheap.2020.02.009](https://doi.org/10.1016/j.jheap.2020.02.009)
- Liao, J.-Y., Zhang, S., Chen, Y., et al. 2020, *Journal of High Energy Astrophysics*, 27, 24, doi: [10.1016/j.jheap.2020.02.010](https://doi.org/10.1016/j.jheap.2020.02.010)
- Liu, C. Z., Zhang, Y. F., Li, X. F., et al. 2020, *Sci. China-Phys. Mech. Astron.*, 63(4): 249503. <https://arxiv.org/abs/1910.04955>
- Liu, J. F., McClintock, J. E., Narayan, R., Davis, S. W., & Orosz, J. A. 2008, *ApJ*, 679, L37, doi: [10.1086/588840](https://doi.org/10.1086/588840)
- Makishima, K., Maejima, Y., Mitsuda, K., et al. 1986, *ApJ*, 308, 635, doi: [10.1086/164534](https://doi.org/10.1086/164534)
- Matsuoka, M., Kawasaki, K., Ueno, S., et al. 2009, *PASJ*, 61, 999, doi: [10.1093/pasj/61.5.999](https://doi.org/10.1093/pasj/61.5.999)
- McClintock, J. E., Shafee, R., Narayan, R., et al. 2006, *ApJ*, 652, 518, doi: [10.1086/508457](https://doi.org/10.1086/508457)
- Mitsuda, K., Inoue, H., Koyama, K., et al. 1984, *PASJ*, 36, 741
- Morningstar, W. R., Miller, J. M., Reis, R. C., & Ebisawa, K. 2014, *ApJL*, 784, L18, doi: [10.1088/2041-8205/784/2/L18](https://doi.org/10.1088/2041-8205/784/2/L18)
- Noble, S. C., Krolik, J. H., & Hawley, J. F. 2009, *ApJ*, 692, 411, doi: [10.1088/0004-637X/692/1/411](https://doi.org/10.1088/0004-637X/692/1/411)
- . 2010, *ApJ*, 711, 959, doi: [10.1088/0004-637X/711/2/959](https://doi.org/10.1088/0004-637X/711/2/959)
- Noble, S. C., Krolik, J. H., Schnittman, J. D., & Hawley, J. F. 2011, *ApJ*, 743, 115, doi: [10.1088/0004-637X/743/2/115](https://doi.org/10.1088/0004-637X/743/2/115)
- Novikov, I. D., & Thorne, K. S. 1973, in *Black Holes (Les Astres Occlus)*, 343–450
- Penna, R. F., McKinney, J. C., Narayan, R., et al. 2010, *MNRAS*, 408, 752, doi: [10.1111/j.1365-2966.2010.17170.x](https://doi.org/10.1111/j.1365-2966.2010.17170.x)
- Remillard, R. A., & McClintock, J. E. 2006, *ARA&A*, 44, 49, doi: [10.1146/annurev.astro.44.051905.092532](https://doi.org/10.1146/annurev.astro.44.051905.092532)
- Reynolds, C. S., & Fabian, A. C. 2008, *ApJ*, 675, 1048, doi: [10.1086/527344](https://doi.org/10.1086/527344)
- Reynolds, C. S., & Nowak, M. A. 2003, *PhR*, 377, 389, doi: [10.1016/S0370-1573\(02\)00584-7](https://doi.org/10.1016/S0370-1573(02)00584-7)
- Shafee, R., McKinney, J. C., Narayan, R., et al. 2008a, *ApJL*, 687, L25, doi: [10.1086/593148](https://doi.org/10.1086/593148)
- Shafee, R., Narayan, R., & McClintock, J. E. 2008b, *ApJ*, 676, 549, doi: [10.1086/527346](https://doi.org/10.1086/527346)
- Shappee, B. J., Prieto, J. L., Grupe, D., et al. 2014, *ApJ*, 788, 48, doi: [10.1088/0004-637X/788/1/48](https://doi.org/10.1088/0004-637X/788/1/48)
- Shidatsu, M., Nakahira, S., Murata, K. L., et al. 2019, *ApJ*, 874, 183, doi: [10.3847/1538-4357/ab09ff](https://doi.org/10.3847/1538-4357/ab09ff)
- Steiner, J. F., McClintock, J. E., Orosz, J. A., et al. 2014, *ApJ*, 793, L29, doi: [10.1088/2041-8205/793/2/L29](https://doi.org/10.1088/2041-8205/793/2/L29)
- Steiner, J. F., McClintock, J. E., & Reid, M. J. 2012, *ApJL*, 745, L7, doi: [10.1088/2041-8205/745/1/L7](https://doi.org/10.1088/2041-8205/745/1/L7)
- Steiner, J. F., McClintock, J. E., Remillard, R. A., Narayan, R., & Gou, L. 2009a, *ApJL*, 701, L83, doi: [10.1088/0004-637X/701/2/L83](https://doi.org/10.1088/0004-637X/701/2/L83)
- Steiner, J. F., Narayan, R., McClintock, J. E., & Ebisawa, K. 2009b, *PASP*, 121, 1279, doi: [10.1086/648535](https://doi.org/10.1086/648535)
- Steiner, J. F., Walton, D. J., García, J. A., et al. 2016, *ApJ*, 817, 154, doi: [10.3847/0004-637X/817/2/154](https://doi.org/10.3847/0004-637X/817/2/154)
- Steiner, J. F., Reis, R. C., McClintock, J. E., et al. 2011, *MNRAS*, 416, 941, doi: [10.1111/j.1365-2966.2011.19089.x](https://doi.org/10.1111/j.1365-2966.2011.19089.x)
- Torres, M. A. P., Casares, J., Jiménez-Ibarra, F., et al. 2020, *ApJL*, 893, L37, doi: [10.3847/2041-8213/ab863a](https://doi.org/10.3847/2041-8213/ab863a)
- . 2019, *ApJL*, 882, L21, doi: [10.3847/2041-8213/ab39df](https://doi.org/10.3847/2041-8213/ab39df)
- Tripathi, A., Zhou, M., Abdikamalov, A. B., et al. 2020, *ApJ*, 897, 84, doi: [10.3847/1538-4357/ab9600](https://doi.org/10.3847/1538-4357/ab9600)
- Tucker, M. A., Shappee, B. J., Holdeen, T. W. S., et al. 2018, *ApJL*, 867, L9, doi: [10.3847/2041-8213/aae88a](https://doi.org/10.3847/2041-8213/aae88a)
- Uttley, P., Gendreau, K., Markwardt, C., et al. 2018, *The Astronomer's Telegram*, 11423, 1
- Walton, D. J., Tomsick, J. A., Madsen, K. K., et al. 2016, *ApJ*, 826, 87, doi: [10.3847/0004-637X/826/1/87](https://doi.org/10.3847/0004-637X/826/1/87)
- Wong, T.-W., Valsecchi, F., Fragos, T., & Kalogera, V. 2012, *ApJ*, 747, 111, doi: [10.1088/0004-637X/747/2/111](https://doi.org/10.1088/0004-637X/747/2/111)
- Zhang, S. N., Cui, W., & Chen, W. 1997, *ApJ*, 482, L155, doi: [10.1086/310705](https://doi.org/10.1086/310705)
- Zhang, S. N., Li, T. P., Lu, F. J., et al. 2020, *Sci. China-Phys. Mech. Astron.*, 63(4): 249502, doi: [10.1007/s11433-019-1432-6](https://doi.org/10.1007/s11433-019-1432-6)
- Zhao, X.-S., Dong, Y.-T., Gou, L.-J., et al. 2020, *Journal of High Energy Astrophysics*, 27, 53, doi: [10.1016/j.jheap.2020.03.001](https://doi.org/10.1016/j.jheap.2020.03.001)